




# Methionine metabolite spermidine inhibits tumor pyroptosis by enhancing MYO6-mediated endocytosis

Received: 5 June 2024

Accepted: 19 February 2025

Published online: 04 March 2025



Jiawei Wu<sup>1,2,5</sup>, Cong Ding<sup>1,3,5</sup>, Chuqing Zhang<sup>1,4,5</sup>, Zhimin Xu<sup>1,4</sup>, Zhenji Deng<sup>1,4</sup>, Hanmiao Wei<sup>1,4</sup>, Tingxiang He<sup>1,4</sup>, Liufen Long<sup>1</sup>, Linglong Tang<sup>1,4</sup> , Jun Ma<sup>1,4</sup>  & Xiaoyu Liang<sup>1,4</sup> 

The connection between amino acid metabolism and pyroptosis remains elusive. Herein, we screen the effect of individual amino acid on pyroptosis and identify that methionine inhibits GSDME-mediated pyroptosis. Mechanistic analyses unveil that MYO6, a unique actin-based motor protein, bridges the GSDME N-terminus (GSDME-NT) and the endocytic adaptor AP2, mediating endolysosomal degradation of GSDME-NT. This degradation is increased by the methionine-derived metabolite spermidine noncanonically by direct binding to MYO6, which enhances MYO6 selectivity for GSDME-NT. Moreover, combination targeted therapies using dietary or pharmacological inhibition in methionine-to-spermidine metabolism in the tumor promotes pyroptosis and anti-tumor immunity, leading to a stronger tumor-suppressive effect in in vivo models. Clinically, higher levels of tumor spermidine and expression of methionine-to-spermidine metabolism-related gene signature predict poorer survival. Conclusively, our research identifies an unrecognized mechanism of pyroptotic resistance mediated by methionine-spermidine metabolic axis, providing a fresh angle for cancer treatment.

Pyroptosis is a form of gasdermin family-mediated programmed cell death characterized by pore formation, cell swelling, cytolysis and the release of proinflammatory factors<sup>1,2</sup>. Gasdermin E (GSDME) serves as a main pyroptotic executioner in tumor cells<sup>3</sup>. Induction of GSDME-mediated pyroptosis can not only overcome the apoptosis resistance of tumor cells but also provoke an inflammatory response in tumor microenvironment (TME) and consequently a potent anti-tumor immunity<sup>4–6</sup>. Currently, numerous approaches for induction and activation of GSDME have been devised, but may not always yield a desired outcome due to the fact that gasdermin cleavage does not inevitably lead to cell death. Generally, once gasdermin is cleaved, it generates an

active fragment that undergoes membrane targeting and oligomerization, resulting in the formation of pores<sup>1</sup>. Subsequently, these pore damages trigger a series of membrane repair mechanisms<sup>7,8</sup>. The fate of cell hinges on the delicate balance between the accumulation of membrane damages and the rate of damage repair. Upon disruption of this balance, the cell ultimately succumbs to demise<sup>9</sup>. Thus, it is crucial to comprehend the mechanism that regulates downstream events following GSDME cleavage in order to improve its effectiveness as an anti-tumor therapy.

Pyroptosis has a close relationship with metabolic homeostasis, as demonstrated by the fact that pyroptosis-associated pathways can be

<sup>1</sup>State Key Laboratory of Oncology in South China, Collaborative Innovation Center of Cancer Medicine, Guangdong Key Laboratory of Nasopharyngeal Carcinoma Diagnosis and Therapy, Guangdong Provincial Clinical Research Center for Cancer, Sun Yat-sen University Cancer Center, Guangzhou 510060, P. R. China. <sup>2</sup>Department of Pathology, Sun Yat-Sen University Cancer Center, Guangzhou 510060, P. R. China. <sup>3</sup>Department of Ultrasound and Electrocardiogram, Sun Yat-Sen University Cancer Center, Guangzhou 510060, P. R. China. <sup>4</sup>Department of Radiation Oncology, Sun Yat-sen University Cancer Center, Guangzhou 510060, P. R. China. <sup>5</sup>These authors contributed equally: Jiawei Wu, Cong Ding, Chuqing Zhang. ✉ e-mail: [tangll@sysucc.org.cn](mailto:tangll@sysucc.org.cn); [majun2@mail.sysu.edu.cn](mailto:majun2@mail.sysu.edu.cn); [liangxy1@sysucc.org.cn](mailto:liangxy1@sysucc.org.cn)

regulated by multiple metabolic signals<sup>10</sup>. Examples include  $\alpha$ -KG, whose elevated level inside tumor cells triggers pyroptosis via activating caspase-8-mediated cleavage of Gasdermin C<sup>11</sup>. Besides, execution of pyroptosis can be directly modified by metabolites, such as fumarate which mediates succination of Gasdermin D to prevent its activation<sup>12</sup>. Thus, promotion of tumor pyroptosis via targeting small-molecule metabolite metabolism is worth in-depth investigation.

Tumor cells reprogram their amino acid (AA) metabolism to gain a survival benefit under stress conditions<sup>13,14</sup>. Beyond their fundamental role as energy and biosynthesis sources, amino acids and their derivatives can act as signaling molecules, regulating a variety of biological processes<sup>14,15</sup>. However, the influence of various amino acid metabolisms remains unclear. In this study, we build a pyroptotic cell model to investigate the influence of individual amino acid on pyroptosis and find that Met-derived metabolite SPD attenuates Myosin 6 (MYO6)-mediated endocytic repair of GSDME-NT, thereby antagonizing GSDME-mediated pyroptosis.

## Results

### Methionine restriction promotes GSDME-mediated pyroptosis

Amino acid metabolism is reprogrammed in tumor cells to maintain their survival against various stresses<sup>13</sup>. To investigate the potential link between amino acid metabolism and pyroptosis, we engineered a cell model tailored for the specific induction of GSDME-mediated pyroptosis. Specifically, we fused the N-terminal fragment of human GSDME (GSDME-NT, residues 1-270) with the green fluorescent protein (GFP) at its C-terminus. This construct was integrated into a vector hosting a Tet-On component, enabling doxycycline (Dox)-dependent control over the expression of the fusion protein. Subsequently, this GSDME-NT induction system was stably expressed in HONE-1 (nasopharyngeal carcinoma, NPC) and HCT116 (colorectal carcinoma, CC) cell lines (GSDME-NT<sup>Tet-On</sup> HONE1 and HCT116) (Fig. 1A). To confirm the effectiveness and sensitivity of the model, we conducted a series of tests using cell models which expressed human full-length GSDME (GSDME-FL) fused with GFP upon Dox treatment as a control. Light microscopy revealed a distinct pyroptotic morphology solely in cells expressing GSDME-NT (Figure S1A). Moreover, only GSDME-NT induction resulted in pore formation and cytolysis, as evidenced by elevated propidium iodide (PI) uptake and lactate dehydrogenase (LDH) release (Fig. 1A, Figures S1B–S1D). In accord with these findings, confocal microscopy showed that GSDME-NT primarily localized to the plasma membrane and induced PI staining in a time-dependent manner, while GSDME-FL remained ubiquitously distributed within the cell (Figure S1E). Together, these data suggest that the GSDME-NT induction system allows us to perform high-confidence screening for specific factors that affect GSDME-mediated pyroptosis.

To screen the effect of individual AA metabolism on GSDME-mediated pyroptosis, we deprived GSDME-NT<sup>Tet-On</sup> HONE1 and HCT116 cells of individual AA 12 h before Dox treatment. Assessing PI uptake and LDH release, we found that short-term individual AA deprivation alone did not elevate cell death (Figs. 1B and 1C). Notably, deprivation of Met most significantly augmented Dox-induced PI uptake and LDH release, while the absence of other AAs had relatively minimal or no impact on pyroptosis (Figs. 1B and 1C). Concurrently, we observed that Met deprivation amplified caspase-3 cleavage under GSDME-NT induction (Fig. 1D). To circumvent the influence of endogenous GSDME cleavage by activated caspase-3, GSDME-NT<sup>Tet-On</sup> cells were co-treated with Met-omitted medium and the caspase-3 inhibitor zDEVD-FMK prior to Dox treatment. Under these conditions, caspase-3 inhibition did not reduce PI uptake or LDH release (Fig. 1D–1F). Furthermore, using chemotherapeutic drug cisplatin (DDP) to induce pyroptosis<sup>3</sup>, we confirmed that Met deprivation also promoted pyroptosis driven by endogenous activation of GSDME (Figures S1F–S1H).

Next, we verify the role of Met in modulating GSDME-mediated pyroptosis in vivo. Initially, we verified that compared to a control diet

(0.86% Met), Met restriction diet (MRD, 0.12% Met)<sup>16</sup> effectively reduced serum Met levels (Fig. 1G) without inducing noticeable abnormalities in BALB/c-nu/nu mice. Thereafter, we constructed a transgenic HONE1 cell line, capable of Dox-induced knockdown of endogenous GSDME (GSDME-sh<sup>Tet-On</sup> HONE1), and subcutaneously injected it into the flank of BALB/c-nu/nu mice to establish an ectopic implantation model. We assessed the release of nuclear HMGB1, a recognized marker of pyroptosis<sup>1</sup>, via immunofluorescence in mouse tumors. Intriguingly, MRD significantly increased the proportion of nuclear HMGB1-negative tumor cells during cisplatin treatment (Figs. 1H and 1I). However, this phenotype was counteracted by Dox-induced GSDME knockdown (Figs. 1H and 1I). These findings collectively suggest that Met restriction augments GSDME-mediated pyroptosis.

### Met-derived metabolite SPD mediates pyroptotic resistance

Met is pivotal to intracellular methylation processes as it is the exclusive progenitor of S-adenosylmethionine (SAM), the universal methyl group donor<sup>17,18</sup>. Recognizing that Met deficiency can disrupt SAM-dependent histone methylation<sup>19,20</sup>, we examined vital histone methylation markers and observed a notable decrease in H3k4me3 and H3k9me2 levels in both cell lines following Met deprivation (Figure S2A). Employing MM-102 TFA and BRD4770 to attenuate H3k4me3 and H3k9me2 respectively, we found that PI uptake and LDH release remained largely unchanged by H3k4me3 inhibition, but were suppressed by H3k9me2 inhibition (Figures S2B and S2C). Moreover, concurrent inhibition demonstrated a protective effect against pyroptosis (Figures S2B and S2C). This suggests that the observed alterations in histone methylation status may not contribute to the enhancement of pyroptosis by Met deprivation.

Beyond mediating SAM-dependent reactions, Met also orchestrates multiple biological processes via its metabolic derivatives (Fig. 2A)<sup>18</sup>. High-performance liquid chromatography-mass spectrometry (HPLC-MS) assay demonstrated that Met deprivation resulted in decreased levels of metabolites within the transsulfuration and polyamine synthesis pathways (Fig. 2B). To screen out which metabolic pathway is involved in pyroptotic regulation during Met deprivation, we supplemented the Met-omitted medium with S-adenosylhomocysteine (SAH), SPD and spermine (SPM) and found that only SPD rescue mitigated Dox-induced pyroptosis (Figs. 2C and 2D). Furthermore, inhibiting SPD production via 2-difluoromethylornithine (DFMO), an ornithine decarboxylase (ODC) inhibitor, or *adenosylmethionine decarboxylase* (*AMD1*) or *spermidine synthase* (*SRM*) knockdown (Figures S2D and S2E) resulted in increased PI uptake and LDH release (Fig. 2E–2H). The influence of SPD on DDP-induced pyroptosis was also confirmed through *SRM* knockdown (Figures S2F and S2G). Collectively, these findings support that Met restriction promotes GSDME-mediated pyroptosis via dampening SPD synthesis.

### SPD enhances endolysosomal degradation of GSDME-NT

To explore the underlying mechanism by which SPD regulates GSDME-mediated pyroptosis, we conducted immunoblot and qPCR assays. Our finding revealed that Met deficiency resulted in an increased GSDME-NT protein level, this effect was counteracted by SPD, rather than SPM (Fig. 3A). However, these treatments did not alter GSDME-NT transcriptional level (Fig. 3B), suggesting that SPD might modulate the degradation rate of GSDME-NT. This hypothesis was further corroborated by a cycloheximide (CHX)-chase assay, which demonstrated an enhanced stability of GSDME-NT in the context of the intracellular SPD level diminished by Met deprivation (Figs. 3C and 3D). We also detected the degradation rate of GSDME-FL during Met deficiency and found that it did not alter significantly (Figures S3A and S3B). These data underscored that SPD deficiency promotes pyroptosis via lowering GSDME-NT stability.

GSDME-NT is generated in cytoplasm as a monomer to target cell membrane, and then undergoes oligomerization to form pyroptotic pores<sup>2</sup>. We then investigate which specific form of GSDME-NT was

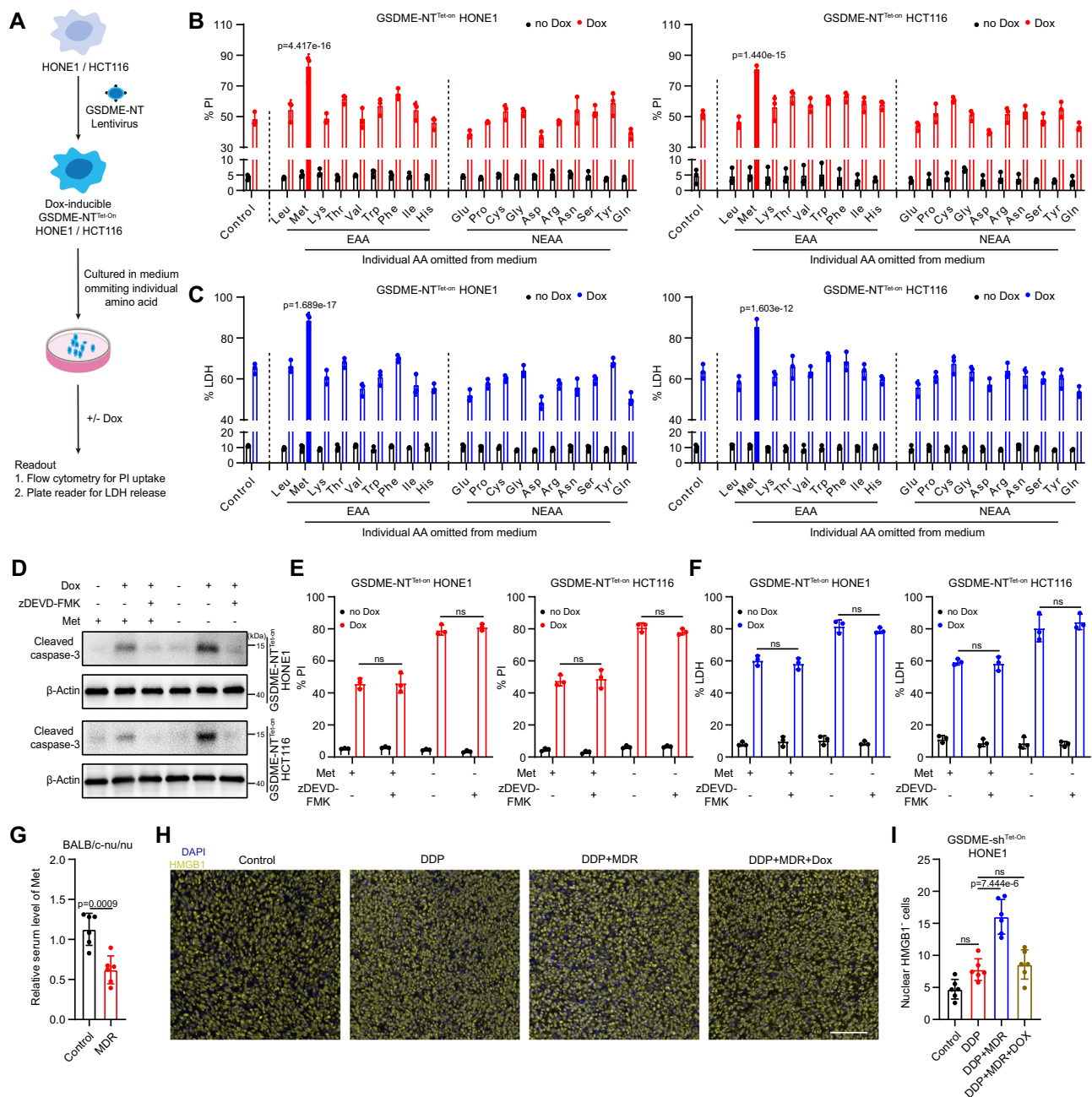


**Fig. 1 | Methionine restriction promotes GSDME-mediated pyroptosis.**

(A) Schematic depicting the workflow for model-building and the screening method. (B and C) Effects of individual amino acid deprivation on Dox-induced PI uptake (B) and LDH release (C) in GSDME-NT<sup>Tet-on</sup> HONE1 and HCT116. EAA, essential amino acid; NEAA, non-essential amino acid. (D) Immunoblot of cleaved caspase-3 in Dox-treated GSDME-NT<sup>Tet-on</sup> HONE1 and HCT116 cultured in normal or Met-omitted medium with or without ZDEVD-FMK (30 μM) treatment. (E and F) Effects of zDEVD-FMK on PI uptake (E) and LDH release (F) in Dox-treated GSDME-NT<sup>Tet-on</sup> HONE1 and HCT116 cultured with normal or Met-omitted medium. All p-values comparing the uptake of PI and the release of LDH in cells subjected to Met

deficiency, in response to Dox, with those in cells subjected to deficiency of other amino acids, are less than 0.0001. (G) Effects of MRD on serum Met level of BALB/c-nu/nu mice (n = 6). (H) Immunofluorescence of HMGB1 in GSDME-sh<sup>Tet-on</sup> HONE1 tumors of indicated groups. Scale bar: 100 μm. (I) Quantification of nuclear HMGB1+ cells shown in (H) (n = 6). Data are represented as mean ± SD. Two-way ANOVA with Bonferroni's multiple comparisons test (B, C, E, F); Two-tailed Student's *t* test (G); One-way ANOVA with Tukey's multiple comparisons test (I). NS, not significant. The results are representative of three independent experiments (B–F). Source data are provided as a Source Data file.

affected by Met deficiency. T6E mutation and F2A plus K40A mutation in GSDME-NT can inhibit its oligomerization in plasma membrane and plasma membrane targeting respectively (Figure S3C)<sup>21,22</sup>. We engineered Tet-On cell models featuring these two GSDME-NT mutants (T6E and F2A plus K40A), neither of which displayed pyroptosis with Dox treatment (Figures S3D and S3E). In consistency with previous reports, immunofluorescence displayed T6E and F2A plus K40A mutants to be monomeric, distributed throughout the cytoplasm, with

T6E additionally targeting the cell membrane (Figure S3F). Of note, the degradation rate of two GSDME-NT mutants remained unchanged in response to Met deprivation (Figures S3G and S3H). Moreover, we observed an increase in oligomer level of GSDME-NT in such settings (Fig. 3E). These findings indicate that Met deficiency primarily enhances the stability of the oligomeric form of GSDME-NT, without significantly impacting the stability of its monomeric form in the cytoplasm or cell membrane.

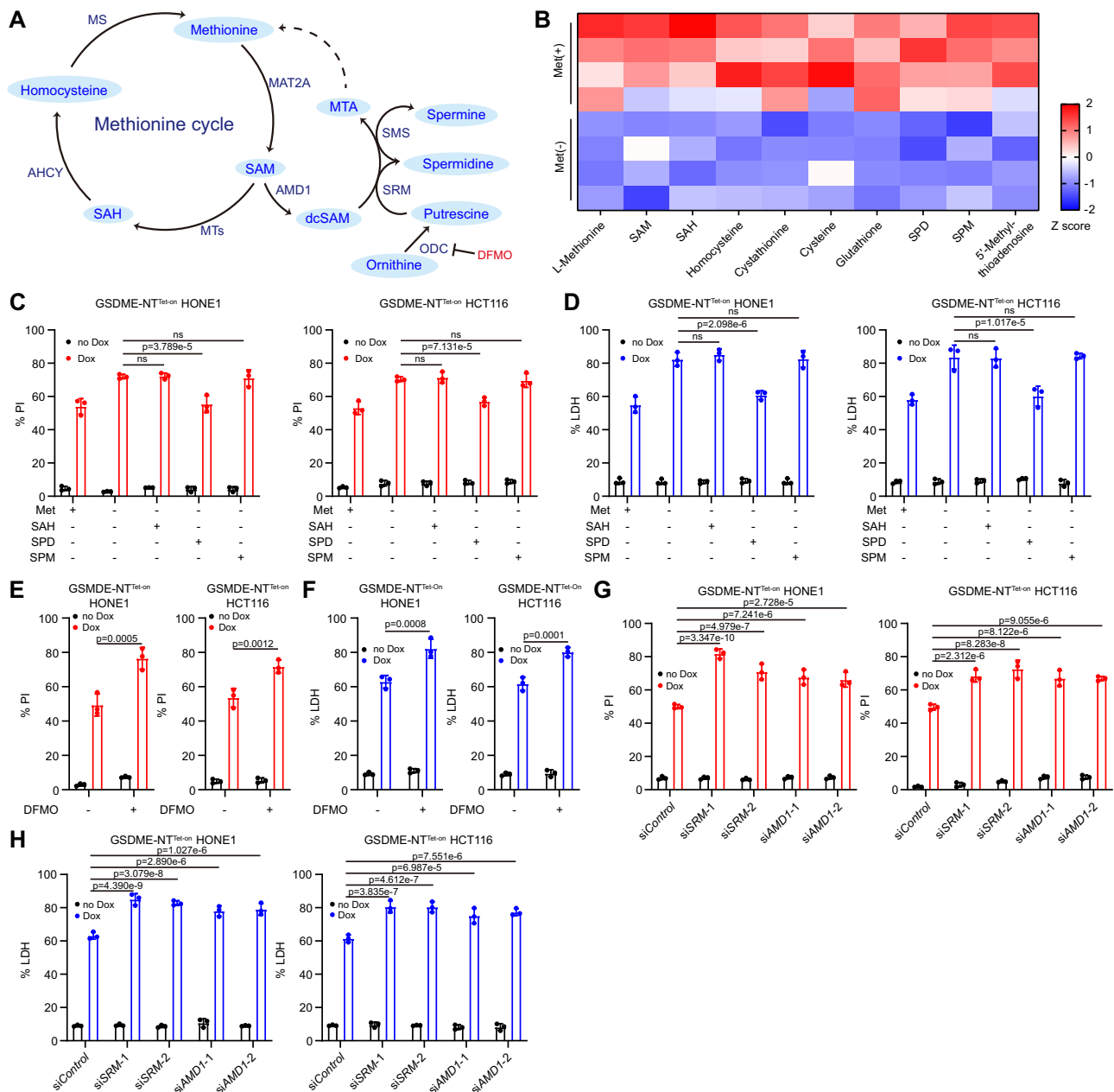


**Fig. 2 | Met-derived metabolite SPD mediates pyroptotic resistance.**

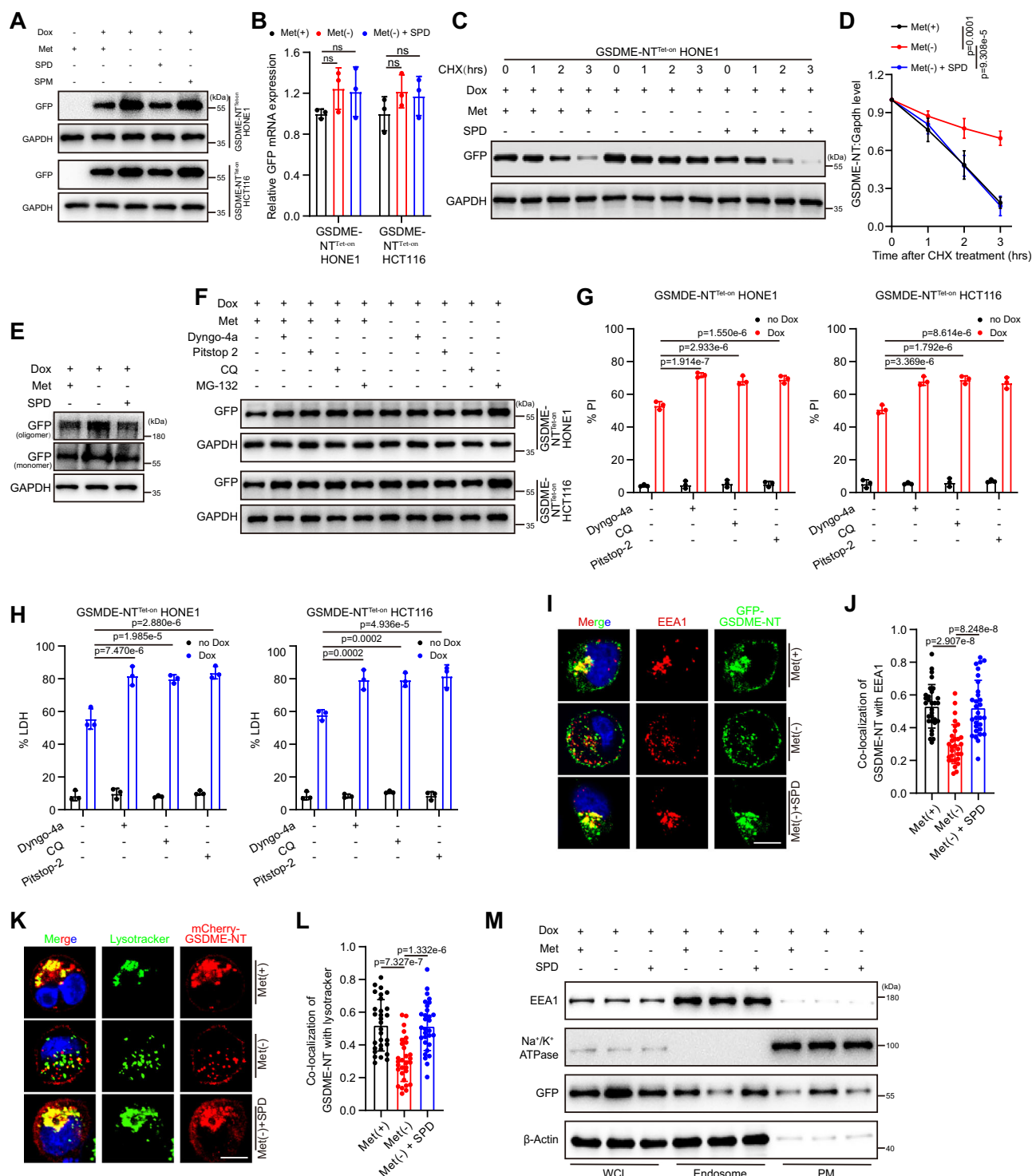
(A) Methionine metabolism schematic. (B) Heatmap of changed metabolites in HONE1 with or without Met deprivation ( $n = 4$ ). (C and D) Effects of addition of SAH (10  $\mu$ M), SPD (50  $\mu$ M), SPM (50  $\mu$ M) on Dox-induced PI uptake (C) and LDH release (D) in GSDME-NT<sup>Tet-on</sup> HONE1 and HCT116 starved of Met. (E and F) Effects of DFMO (500  $\mu$ M) on Dox-induced PI uptake (E) and LDH release (F) in GSDME-NT<sup>Tet-on</sup>

on HONE1 and HCT116. (G and H) Effects of SRM or AMD1 knockdown on Dox-induced PI uptake (G) and LDH (H) release in GSDME-NT<sup>Tet-on</sup> HONE1 and HCT116. Data are represented as mean  $\pm$  SD. Two-way ANOVA with Bonferroni's multiple comparisons test (C–H). NS, not significant. The results are representative of three independent experiments (C–H). Source data are provided as a Source Data file.

The endocytic pathway serves as a crucial conduit for the transport of plasma membrane proteins to the lysosome for degradation<sup>23</sup>. This endolysosomal degradation mechanism also engages in repairing membrane damages, such as streptolysin O-containing pores<sup>7,24</sup>. To identify whether endocytosis is involved in degradation of GSDME-NT oligomers, we suppressed the endolysosomal pathway with endocytosis inhibitor dyngo-4a and lysosomal acidification inhibitor chloroquine (CQ). Both of them led to an increase in GSDME-NT protein level (Fig. 3F) and an enhancement of pyroptosis under conditions of Dox-induced expression of GSDME-NT (Figs. 3G and 3H) and DDP-activated GSDME cleavage (Figure S3I and S3J). Moreover, the application of clathrin inhibitor Pitstop-2 to inhibit clathrin-mediated

endocytosis, a key manner that transports a wide range of cargo molecules from cell membrane to the interior, also induce similar phenotypes (Fig. 3F–3H, Figure S3I and S3J). Subsequent immunofluorescence analysis demonstrated the co-localization of GSDME-NT with early endosomes indicated by EEA1 (Fig. 3I). Another marker of early endosome, Rab5, also colocalized with GSDME-NT (Figures S3K), reconfirming that GSDME-NT could be endocytosed. Additionally, we observed the transfer of GSDME-NT into lysosomes, which were labeled with lysotracker (Fig. 3K). These observations confirm the engagement of the endolysosomal pathway in the degradation of GSDME-NT. Meanwhile, we discovered that Met deprivation could result in a decreased colocalization of GSDME-NT with early endosome





and lysosome, a situation that can be remedied by SPD supplementation (Fig. 3I–3L, Figure S3K and S3L). Similarly, *SRM* knockdown dampened their colocalization (Figures S3M and S3N). We further performed an isolation of early endosome and plasma membrane protein assay and observed a reduction in GSDME-NT protein level within the endosome upon disruption of SPD synthesis by Met deprivation (Fig. 3M) or *SRM* knockdown (Figure S3O). These modifications were not attributed to a decrease in its level within the plasma membrane. Collectively, these findings suggest that SPD promotes the endocytosis of GSDME-NT.

We also detected whether the proteasome pathway regulate GSDME-NT degradation in response to Met deprivation. Immunoblot

displayed that the proteasome inhibitor MG-132 led to an increase in GSDME-NT protein level (Fig. 3F). Of note, unlike that of endolysosomal inhibitors, this effect could be further enhanced by Met deprivation (Fig. 3F), suggesting that Met deficiency do not modulate the proteasome pathway for GSDME-NT degradation.

### SPD directly interacts with MYO6 to regulate endocytosis of GSDME-NT

The canonical cellular function of SPD is to serve as a substrate for hypusination of eukaryotic translation initiation factor 5A (eIF5A) to regulate translation of open reading frames encoding short polyproline tracks (Figure S4A)<sup>25,26</sup>. To validate whether this pathway is

**Fig. 3 | SPD promotes endolysosomal degradation of GSDME-NT.**

(A) Immunoblot of GFP-GSDME-NT in Dox-treated GSDME-NT<sup>Tet-On</sup> HONE1 and HCT116 in response to Met deprivation with or without SPD supplement. (B) Transcriptional level of GFP-GSDME-NT detected by qPCR in Dox-treated GSDME-NT<sup>Tet-On</sup> HONE1 and HCT116 in response to Met deprivation with or without SPD supplement. (C) Immunoblot of GFP-GSDME-NT in Dox-treated GSDME-NT<sup>Tet-On</sup> HONE1 and HCT116 in response to CHX treatment (100 µg/ml) for the indicated time points. (D) Quantification of GFP-GSDME-NT level shown in (C). (E) Immunoblot of GSDME-NT oligomer and monomer in Dox-treated GSDME-NT<sup>Tet-On</sup> HONE1 in response to Met deprivation with or without SPD supplement. (F) Immunoblot of GFP-GSDME-NT in Dox-treated GSDME-NT<sup>Tet-On</sup> HONE1 and HCT116 in response to Dyngo4a (30 µM), CQ (50 µM), Pitstop-2 (30 µM) or MG-132 (10 µM) with or without Met deprivation. (G and H) Effects of Dyngo-4a, CQ and Pitstop-2 on Dox-induced PI uptake (G) and LDH release (H) in GSDME-NT<sup>Tet-On</sup>

HONE1 and HCT116. (I) Immunofluorescence of GFP-GSDME-NT and EEA1 in Dox-treated GSDME-NT<sup>Tet-On</sup> HONE1 in response to Met deprivation with or without SPD supplement. Scale bar: 10 µm. (J) Quantification of colocalization of GFP-GSDME-NT with EEA1 ( $n = 30$  cells) shown in (I). (K) Immunofluorescence of GFP-GSDME-NT and lysotracker in Dox-treated GSDME-NT<sup>Tet-On</sup> HONE1 in response to Met deprivation with or without SPD supplement. Scale bar: 10 µm. (L) Quantification of colocalization of GFP-GSDME-NT with lysotracker ( $n = 30$  cells) shown in (K). (M) Immunoblot of GFP-GSDME-NT of isolated endosomes and plasma membrane in Dox-treated GSDME-NT<sup>Tet-On</sup> HONE1 in response to Met deprivation with or without SPD supplement. WCL, whole cell lysates; PM, plasma membrane. Data are represented as mean  $\pm$  SD. One-way ANOVA with Tukey's multiple comparisons test (B, D, J, L); Two-way ANOVA with Bonferroni's multiple comparisons test (G and H). NS, not significant. The results are representative of three independent experiments (A–M). Source data are provided as a Source Data file.

involved in endocytosis of GSDME-NT, we exposed cells to GC7, a specific inhibitor of deoxyhypusine synthase (DHPS), and observed an inhibition in PI uptake and LDH release following GSDME-NT induction (Figures S4B and S4C). In a parallel vein, genetic silencing of two key hypusination enzymes *DHPS* and *deoxyhypusine hydroxylase (DOHH)* (Figures S4D and S4E) also effectively shielded tumor cells from Dox-induced pyroptosis (Figures S4F and S4G). These findings imply that the regulation of pyroptosis by SPD operates independently from the hypusination of eIF5A.

Considering the ability of SPD to interact with proteins and modulate their function<sup>27</sup>, we postulated that SPD might directly bind to constituents of endocytic complex of GSDME-NT to promote its endocytosis. To validate this hypothesis, NHS beads coated with SPD were constructed to isolate SPD-binding proteins from pyroptotic cell lysates (Fig. 4A). Then, these bound proteins were eluted in a high-salt buffer containing 2-mM SPD and subjected to mass spectrometry (MS) analysis (Figure S4H). Concurrently, we engineered a cell expressing Dox-inducible GSDME-NT with HA-tag at its C-terminus and also detected proteins binding to GSDME-NT from lysates of cells treated with or without Met deprivation (Figure S4I). MS analysis revealed that both SPD and GSDME-NT interacted with MYO6 (Fig. 4B), a unique actin-based motor protein which forms a complex with cargo in cell surface for selective endocytic degradation<sup>28</sup>. Of note, MYO6 was undetectable by MS among GSDME-NT-binding proteins in absence of Met (Fig. 4B). Functionally, *MYO6* knockdown led to an increased protein level of GSDME-NT (Fig. 4C), as well as an enhancement in Dox- and DDP-induced pyroptosis (Figs. 4D and 4E, Figures S4J and S4K). We subsequently confirmed that MYO6 mediates endocytosis of GSDME-NT, as revealed by the reduction in colocalization of GSDME-NT with EEA1 (Figs. 4F and 4G) and endosomal protein level of GSDME-NT (Fig. 4H). Thus, these data suggest that MYO6 potentially operates as a downstream effector of SPD to mediate the endocytosis of GSDME-NT.

Then, to corroborate the interaction between SPD and MYO6, an immunoblot assay was employed to display a competitive reduction in the binding of MYO6 to SPD-coated beads upon the addition of 2 mM SPD into the mixing buffer (Fig. 4I). We further confirmed their direct binding via a series of experiments. The first is cellular thermal shift assay (CETSA), in which the thermal stability of MYO6 protein was increased by their binding with SPD in mixing buffer (Fig. 4J). Subsequently, proximity ligation assay (PLA) demonstrated the detection of specific and discrete fluorescent signals by the interaction of two separate antibodies each to SPD or FLAG tag of MYO6 (Figs. 4K and 4L). Finally, we performed a biolayer interferometry (BLI) assay and observed its binding affinity to SPD with  $K_d$  of  $4.22 \times 10^{-4}$  M (Fig. 4M).

**MYO6 bridges GSDME-NT and the endocytic adaptor AP2**

Our subsequent investigation elucidated the mechanism through which MYO6 modulates GSDME-mediated pyroptosis. Initially, we

validated the influence of SPD on the interaction between MYO6 and GSDME-NT. Co-immunoprecipitation assay demonstrated that the absence of Met resulted in a diminished interaction between MYO6 and GSDME-NT (Fig. 5A), this effect could be reversible upon the SPD addition (Fig. 5A). Likewise, the knockdown of SRM was shown to inhibit their interaction (Figure S5A). Moreover, we observed that MYO6 barely interacted with GSDME-FL (Figure S5B). Next, we pinpoint the binding sites between MYO6 and GSDME-NT. Structurally, MYO6 includes three regions: a N-terminal motor (head) domain (residues 1-771), followed by a neck domain (residues 772-834) consisting of a unique reverse gear and a single IQ motif, and a C-terminal tail region (residues 835-1285) with a three-helix bundle region, a single  $\alpha$ -helix domain and a unique globular domain (CBD, residues 1157-1285) required for interaction with other proteins such as cargo-binding (Fig. 5B)<sup>28,29</sup>. Thus, we generated Flag-tagged MYO6 truncated mutants containing a mCherry tag at their C-terminus (Fig. 5B) and found that GSDME-NT interacted with the CBD of MYO6 (Fig. 5C). Besides, we mutated two canonical protein-protein interaction modules, the RRL and WWY motif, within CBD<sup>28,29</sup>. However, these mutations barely disrupted the interaction with GSDME-NT (Figure S5C).

To further clarify the details of the interaction between MYO6 and GSDME-NT and the alteration of this interaction by SPD, we performed molecular docking and molecular dynamics (MD) simulations. The analysis of root-mean square-deviation (RMSD) revealed that in the presence of SPD, MYO6-GSDME-NT complex formed equilibrium state more easily (Fig. 5D), and the structure of MYO6 but not GSDME-NT became more stable and flexible in MYO6-GSDME-NT complex (Fig. 5E, Figures S5D and S5E). Then, based on Molecular Mechanics Poisson-Boltzmann Surface Area (MMPBSA), we found that the bind free energy of MYO6 with GSDME-NT was shifted by SPD from -48.12 kcal/mol and -165.69 kcal/mol (Supplementary Table 1). Furthermore, consistent with the previous immunoprecipitation results, the residues of MYO6 interacted with GSDME-NT were basically concentrated in its CBD with or without its binding with SPD (Figs. 5F and 5G, Supplementary Tables 2 and 3). The above findings indicate that SPD enhances interaction between MYO6 and GSDME-NT.

Previous reports have demonstrated that MYO6 interacts with endocytic adaptors to regulate cargo degradation<sup>28</sup>. Therefore, we screened for GSDME-NT-specific adaptors by examining the interaction of GSDME-NT with canonical endocytic adaptors, including AP2M1 (subunit Mu 1 of Adaptor Related Protein Complex 2, AP2), Dab2, EPN1, EPN2 and PICALM<sup>30</sup>. CO-IP analysis revealed that AP2M1 primarily interacted with GSDME-NT compared to other adaptors (Figure S5F). Furthermore, *AP2M1* knockdown led to an increase in GSDME-NT levels along with the enhancement of Dox- and DDP-induced pyroptosis (Figures S5G-S5L), and inhibited colocalization of GSDME-NT with EEA1 (Figures S5M and S5N), indicating that AP2M1 mediates the selective endocytic degradation of GSDME-NT.

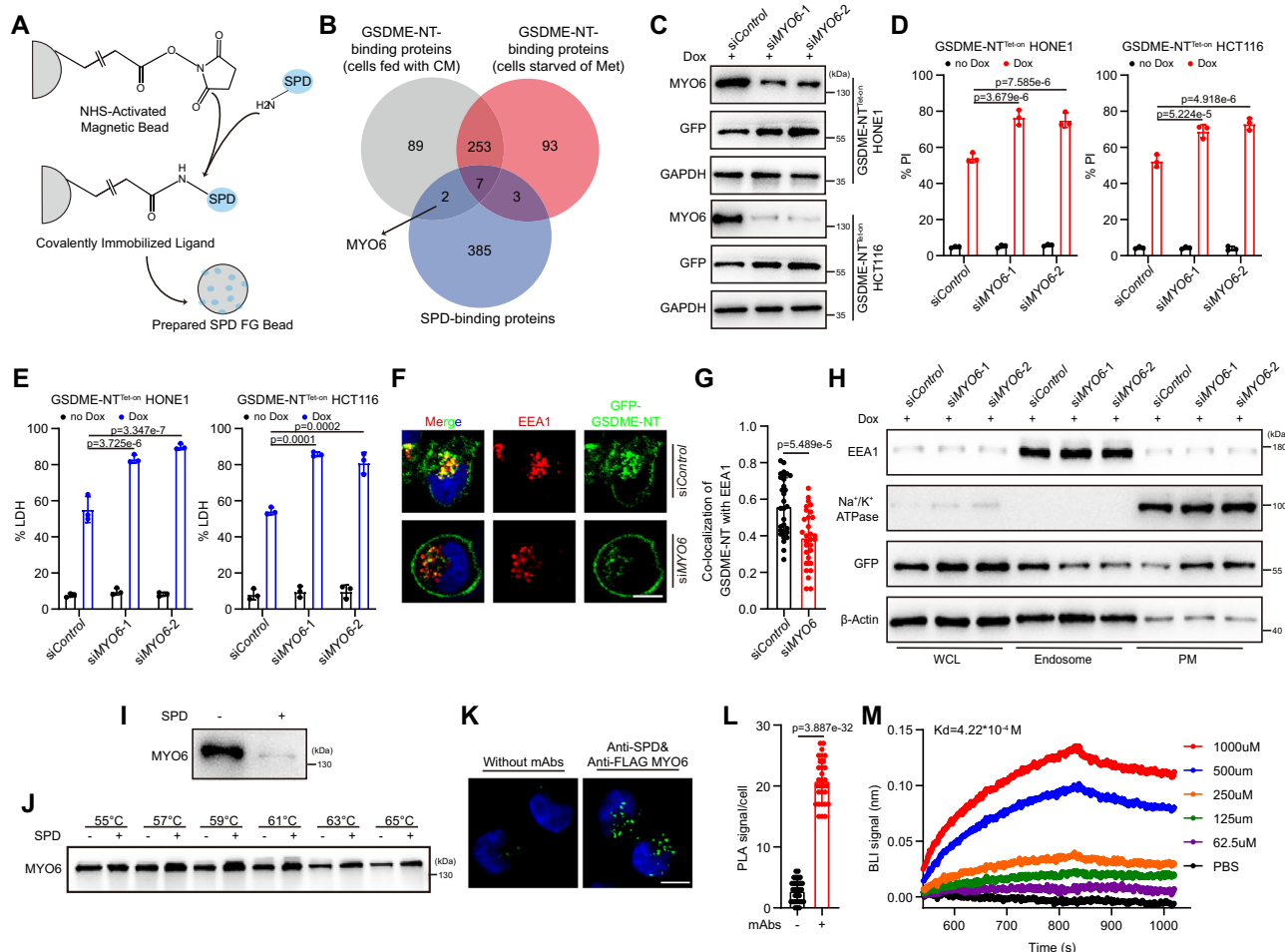


**Fig. 4 | SPD directly interacts with MYO6 to regulate endocytosis of GSDME-NT.**

(A) Schematic depicting the production of SPD FG bead. (B) Venn diagram displaying the intersection among SPD-binding proteins and GSDME-NT-binding proteins (cells fed with CM or Met-omitted medium) in Dox-treated GSDME-NT<sup>Tet-On</sup> HONE1. (C) Immunoblot of GFP-GSDME-NT in Dox-treated GSDME-NT<sup>Tet-On</sup> HONE1 and HCT116 with MYO6 knockdown. (D and E) Effects of MYO6 knockdown on Dox-induced PI uptake (D) and LDH release (E) in GSDME-NT<sup>Tet-On</sup> HONE1 and HCT116. (F) Immunofluorescence of GFP-GSDME-NT and EEA1 in Dox-treated GSDME-NT<sup>Tet-On</sup> HONE1 with MYO6 knockdown. Scale bar: 10  $\mu$ m. (G) Quantification of colocalization of GFP-GSDME-NT with EEA1 ( $n = 30$  cells) shown in (F). (H) Immunoblot of GFP-GSDME-NT of isolated endosomes and plasma membrane in Dox-treated GSDME-

NT<sup>Tet-On</sup> HONE1 with MYO6 knockdown. WCL, whole cell lysates; PM, plasma membrane. (I) High concentration of SPD (2 mM) addition to lysates from Dox-treated GSDME-NT<sup>Tet-On</sup> HONE1 inhibited capture of MYO6 proteins by SPD-conjugated beads. (J) CETSA displaying an increase thermal stability of MYO6 by SPD addition. (K) In situ Duolink-PLA assay displaying the molecular interaction between SPD and MYO6 in Dox-treated GSDME-NT<sup>Tet-On</sup> HONE1. Scale bar: 10  $\mu$ m. (L) Quantification of PLA signal per cell ( $n = 30$  cells) shown in (K). (M) BLI analysis of the molecular binding between SPD and MYO6. Data are represented as mean  $\pm$  SD. Two-way ANOVA with Bonferroni's multiple comparisons test (D and E); Two-tailed Student's  $t$  test (G and L). NS, not significant. The results are representative of three independent experiments (C–L). Source data are provided as a Source Data file.

Subsequently, we detected an interaction between MYO6 and AP2M1 in presence or absence of Met during pyroptosis (Fig. 5H), substantiating a GSDME-NT-MYO6-AP2 triangular interaction. Notably, both MYO6 knockdown and blockage of Met-SPD axis reduced the interaction between AP2M1 and GSDME-NT (Fig. 5I and Figure S50). These findings suggest that MYO6 functions as an adaptor in an on-off ligand-dependent switchable mode, bridging AP2 and GSDME-NT.

### High tumor SPD level and expression of MEPO signature predicts a poor prognosis

Given the profound clinical implications of pyroptosis and the observed inhibitory role of SPD on this process, we further explored the prognostic potential of SPD. Immunohistochemistry (IHC) was employed to ascertain SPD levels in 220 NPC specimens. Based on staining intensity, patients were stratified into groups with high and low SPD levels (Fig. 6A). Our findings revealed a significant association between elevated tumor SPD levels and increased death risk (Fig. 6B). Moreover, Kaplan-Meier analysis identified a high level of SPD as a predictor of poor overall survival (Fig. 6C).

In a subsequent investigation, we sought to determine the clinical relevance of the anti-pyroptotic mechanism associated with Met and SPD metabolism. To this end, we constructed a gene set (MEPO signature) comprising Met salvage pathway- and Polyamine synthesis-related genes (Listed in methods) and conducted a series of analyses using the TCGA database. Corresponding to our aforementioned findings, upregulated expression of MEPO signature was associated with a low score of activated DC (Fig. 6D) and T effector (Teff) cell immunity (Fig. 6E). Furthermore, prognostic analysis revealed a negative correlation between the expression of MEPO signature and survival (Fig. 6F). Altogether, our data explained the potential value of tumor SPD level and MEPO signature in prediction of prognosis.

### SLC7A5 is a potential target of implementing Met restriction therapy

AA transporter targeting is considered a promising strategy of interfering AA metabolism, having the advantage of a higher clinical feasibility in comparison to dietary restriction regimen<sup>31,32</sup>. This prompted



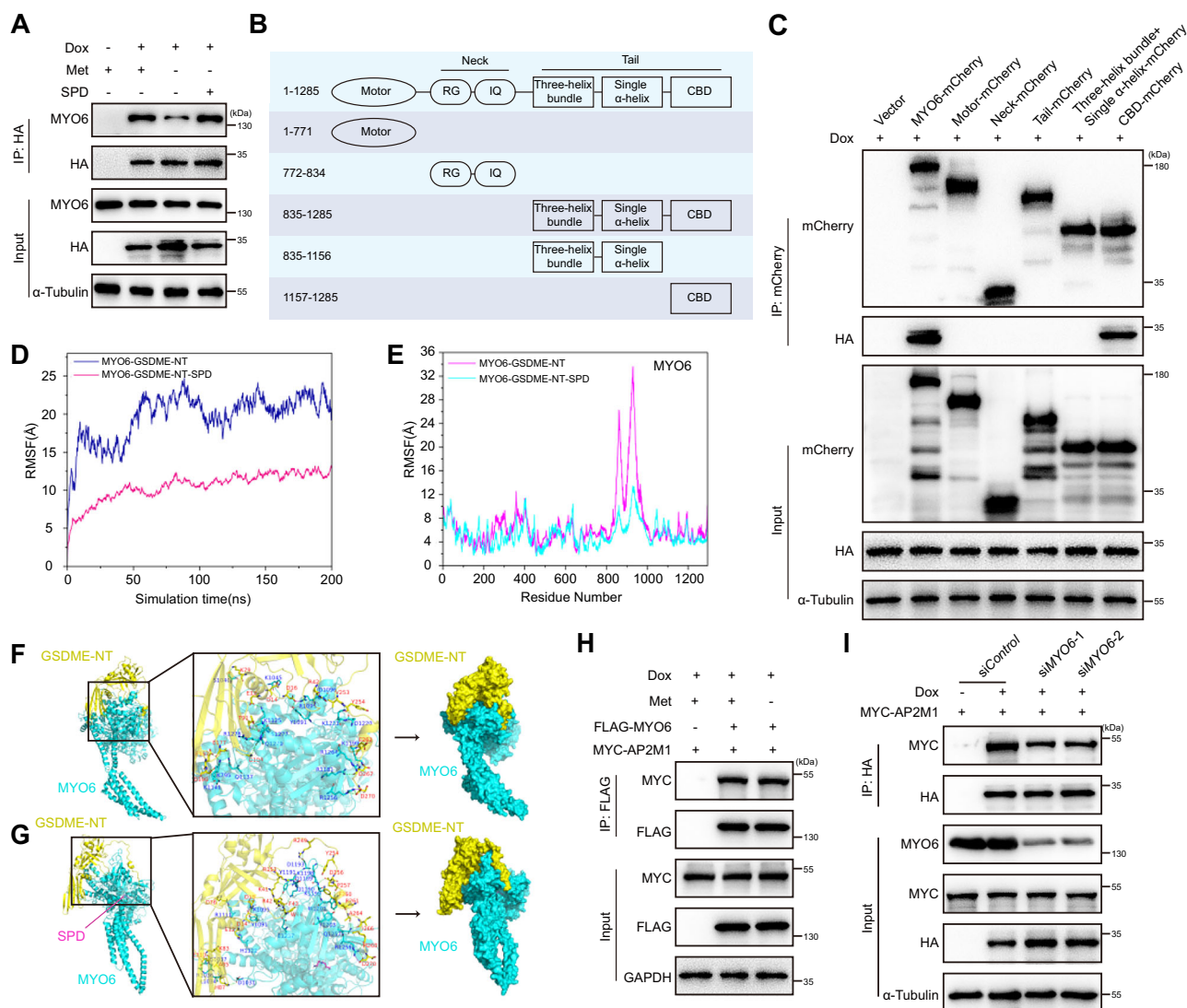


**Fig. 5 | MYO6 bridges GSDME-NT and the endocytic adaptor AP2. (A)** Co-IP with an anti-HA antibody using lysates from Dox-treated GSDME-NT<sup>Tet-On</sup> HONE1 undergoing Met deprivation with or without SPD treatment. **(B)** Schematic of MYO6 and its truncation mutant structure. **(C)** Co-IP with an anti-mCherry antibody using lysates from Dox-treated GSDME-NT<sup>Tet-On</sup> HONE1 with transfection of MYO6 or its truncation mutants. **(D)** The tendency of the root mean square deviation (RMSD) plot for two indicated complexes. **(E)** The RMSF plot for MYO6 in two indicated complexes. **(F and G)** The simulation of the interaction and surface

binding model between MYO6 and GSDME-NT in the absence **(F)** or presence **(G)** of SPD. **(H)** Co-IP with an anti-FLAG antibody using lysates from Dox-treated GSDME-NT<sup>Tet-On</sup> HONE1 with transfection of FLAG-MYO6 and/or MYC-AP2M1 undergoing Met deprivation. **(I)** Co-IP with an anti-HA antibody using lysates from Dox-treated GSDME-NT<sup>Tet-On</sup> HONE1 with transfection of MYC-AP2M1 and MYO6 knockdown. The results are representative of three independent experiments **(A, C, H and I)**. Source data are provided as a Source Data file.

us to find out the major Met transporter of tumor cell. Solute carrier family (SLC), responsible for Met uptake, are divided into system L- and system A-type<sup>33</sup>. Using BCH and MeAIB to inhibit system L- and system A-type transporter respectively, we observed that BCH, but not MeAIB, promoted tumor cells to take up PI and release LDH upon induction of GSDME-NT (Figures S6A and S6B). Thus, our subsequent exploration focused on the system L-type transporters. Employing a q-PCR assay, we found that unlike a previous study which demonstrates a relatively high transcriptional level of SLC7A5, SLC7A6 and SLC43A2 in mouse melanoma<sup>33</sup>, only SLC7A5 had a much higher transcriptional level than other system L-type transporters and was upregulated remarkably after Met deprivation in human NPC and CC cell lines (Figures S6C and S6D), suggesting that SLC7A5 might be a crucial Met transporter of tumor cells. Further experiments demonstrated that JPH203, a high-affinity specific inhibitor of SLC7A5, lowered the intracellular level of Met and SPD (Figure S6E). More importantly, JPH203 enhanced Dox- and DDP-induced pyroptosis

functionally (Figures S6F-S6I), and reduced GSDME-NT protein level as well as the interaction between MYO6 and GSDME-NT mechanistically (Figures S6J). These findings suggest that SLC7A5 could be as a potential target for enhancing tumor pyroptosis.

### Met restriction therapy boosts cetuximab efficacy via enhancing anti-tumor immunity

Nutrition stress results in upregulation of EGFR<sup>34</sup>. Likewise, our findings unveiled that Met starvation could amplify the surface distribution of EGFR (Figure S7A). It is well-established that high surface level of EGFR is proficient in potentiating EGFR monoclonal antibody (mAb)-induced antibody-dependent cell-mediated cytotoxicity (ADCC), which play a crucial role in response to clinical mAb-based therapy<sup>35</sup>. Thus, we speculated that Met restriction therapy (MRT) is potential to enhance Cetuximab (Cmab)-mediated ADCC and promote ADCC-induced pyroptosis. As expected, deleting Met from medium or JPH203 treatment augmented the cytotoxic capacity of human NK



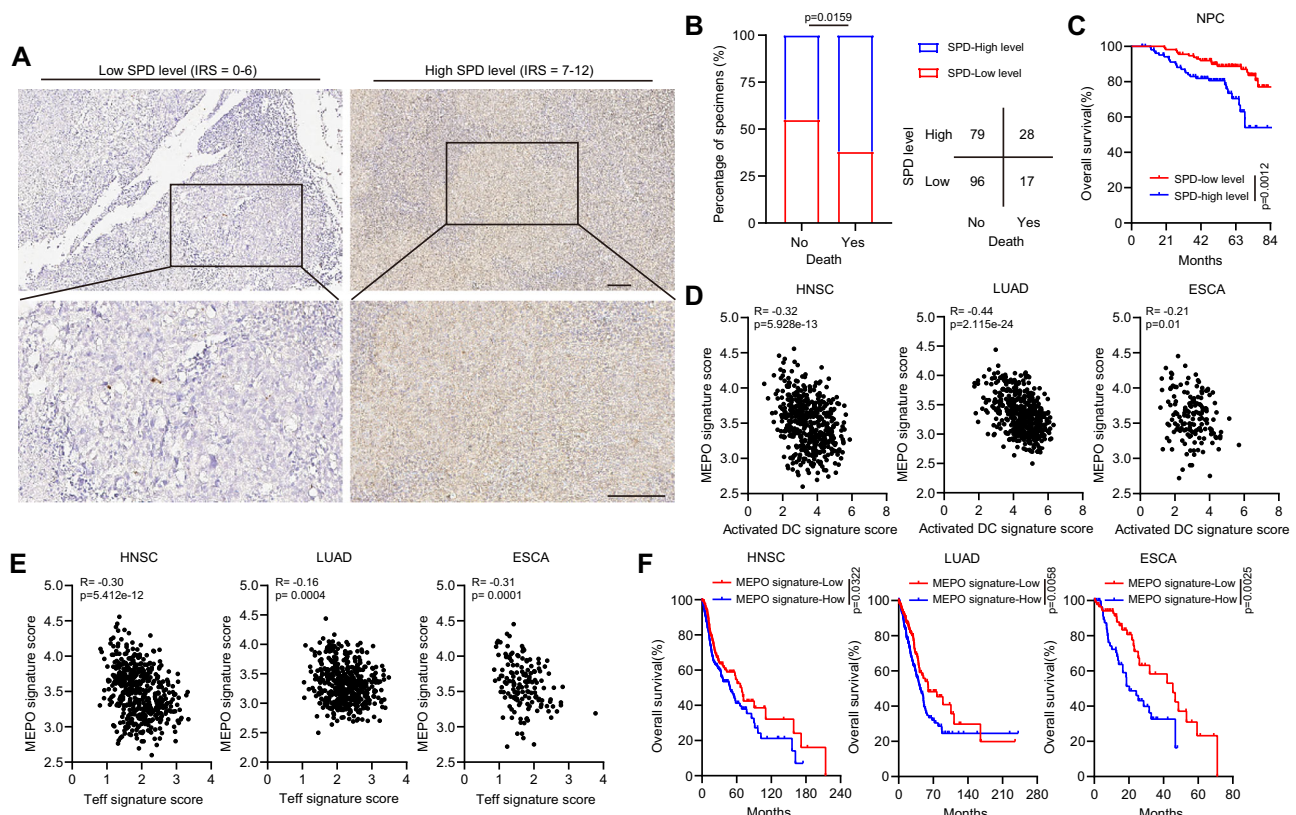


**Fig. 6 | High tumor SPD level and expression of MEPO signature predicts a poor prognosis.** (A) SPD level is evaluated by IHC staining in 220 NPC tumor tissues. Scale bar: 100 $\mu$ m. (B) Association between SPD level and death status in a cohort of 220 NPC samples (two-sided  $\chi^2$  test). (C) Kaplan–Meier analysis of overall survival based on the SPD level (log-rank test). (D) The correlation between MEPO signature expression and activated DC signature expression in head and neck squamous carcinoma (HNSC), lung adenocarcinoma (LUAD) and esophageal carcinoma

(ESCA) (The correlation coefficient and two-tailed  $p$  value were calculated using Pearson's correlation analysis). (E) The correlation between MEPO signature expression and effector T cell signature expression in HNSC, LUAD and ESCA (Pearson's correlation analysis). (F) Kaplan–Meier analysis of overall survival based on the SPD level in HNSC, LUAD and ESCA (log-rank test). Source data are provided as a Source Data file.

cells against HONE1 and HCT116 in the presence of Cmb. This was evidenced by an increased frequency of PI-positive cell (Fig. 7A and Figure S7B). In addition, Cmb-mediated ADCC resulted in the generation of GSDME-NT and the secretion of HMGB1, both of which were found to be elevated under Met restriction (Figs. 7B and 7C, Figures S7C and S7D), indicating that Met deficiency enhanced pyroptosis induced by Cmb-mediated ADCC.

Next, to investigate the *in vivo* implications of combining Cmb with MRD and JPH203 on tumor progression, we established subcutaneous tumors in BALB/c-nu mice utilizing HONE1 cells. Both the MRD and JPH203 treatment resulted in a significant reduction of intratumor Met and SPD levels within HONE1 tumors (Figure S7H). The tumor growth inhibition effect of these treatments was found to be comparable to that of Cmb (Figs. 7D and 7E). Interestingly, the combination of MRD or JPH203 with Cmb resulted in additional tumor suppression (Figs. 7D and 7E). Notably, tumor volume change revealed that the removal of the Fc fragment from Cmb compromised the tumor-suppressive effects of both Cmb and the combination therapy (Figures S7I and S7J). This can be attributed to the inability of Cmb F(ab')<sub>2</sub> to induce ADCC, as it primarily functions in EGFR binding and subsequent signal inhibition<sup>36</sup>. Thus, depriving tumor of Met enhances Cmb-induced ADCC response *in vivo*.

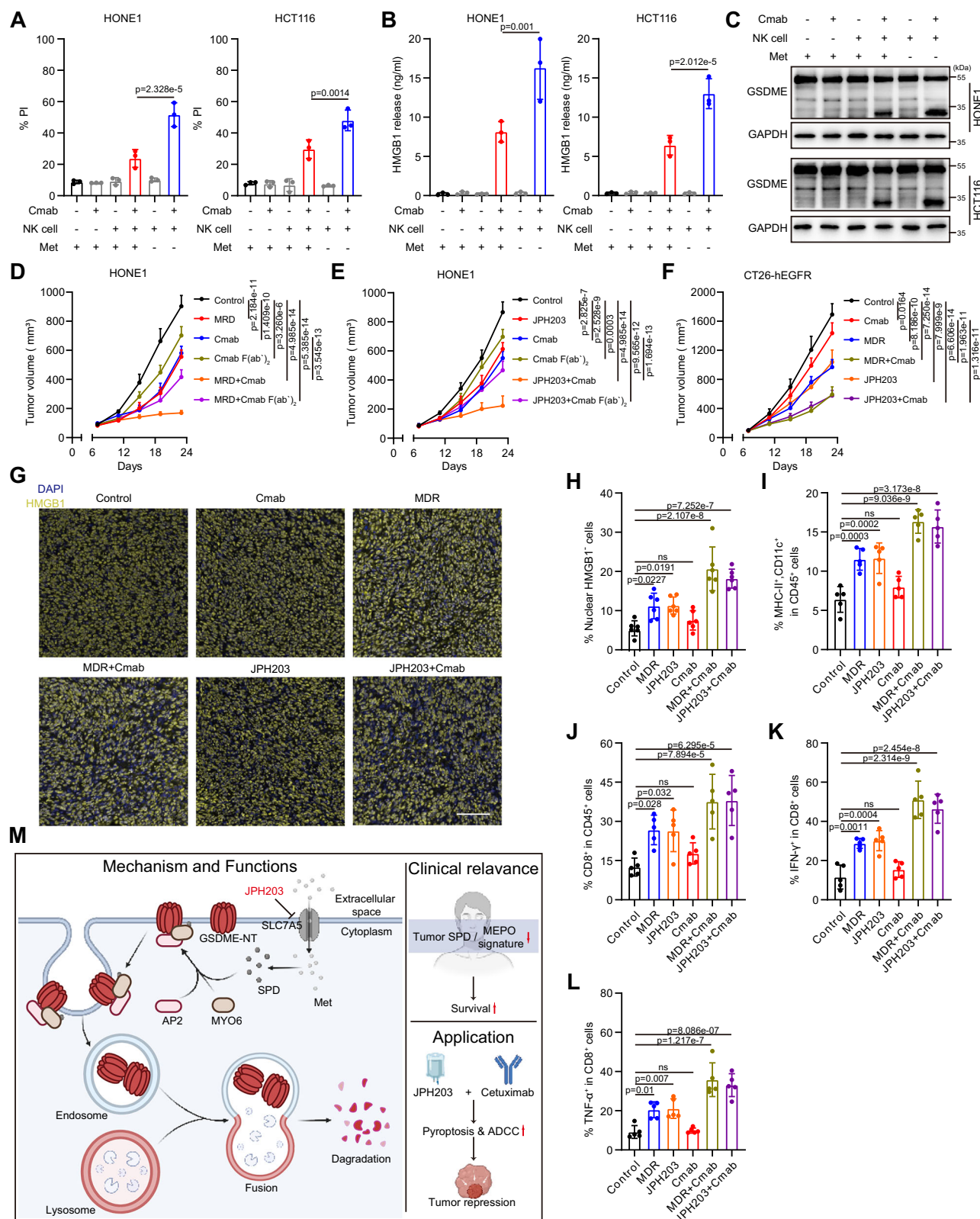
Recognizing the ability of pyroptosis to facilitate the release of DAMPs, which in turn activate dendritic cells (DCs) and subsequently enhance T-cell immunity within the TME<sup>5,37</sup>, we further explored the role of combination therapies in regulating pyroptosis to modulate TME. We generated a CT26-hEGFR cell line stably expressing human

EGFR on its cell surface (Figure S7K), and subcutaneously inoculated this into immunocompetent (BALB/c) mice. We observed that both MRD and JPH203 reduced the levels of Met and SPD (Figure S7L), as well as the growth rate of CT26-hEGFR tumors (Fig. 7F). Moreover, their combination with Cmb resulted in significantly greater impairment of tumor growth compared to Cmb treatment alone (Fig. 7F). Crucially, Met restriction combined with Cmb further promoted the release of HMGB1, infiltration of activated DCs (CD11c<sup>+</sup>, MHC-II<sup>+</sup>) and CD8<sup>+</sup> T cells, and the production of IFN- $\gamma$  and TNF- $\alpha$ , indicatives of improved T-cell function (Fig. 7G–7L). In conclusion, we propose that the combination of Cmb with dietary or pharmacological restrictions on tumor uptake of methionine can enhance both innate and adaptive antitumor immunity, thereby suggesting a novel therapeutic strategy for cancer treatment.

Last but not least, we also validated the synergistic effects of targeting SPD synthesis and EGFR blockade. *In vitro* assays demonstrated that the inhibition of SPD synthesis via DFMO amplified both ADCC and pyroptosis in response to Cmb treatment (Figure S7E–S7G). Furthermore, the combination of DFMO and Cmb significantly alleviated tumor burden in both immunocompetent and immunodeficient mouse models (Figures S7M and S7N). These findings underscore the potential of combining targeted SPD synthesis and EGFR blockade in cancer treatment.

## Discussion

Tumor cells exhibit robust Met metabolism, significantly impacting tumor initiation, growth, and metastasis<sup>38,39</sup>. Yet, the role of Met



metabolism in modulating cell death pattern is not well-characterized. Herein, we demonstrate that MYO6 functions as a bridge connecting GSDME-NT with the endocytic adaptor AP2 to mediate endocytosis of GSDME-NT. Notably, this MYO6-mediated repair mechanism of GSDME-NT pores can be potentiated by SPD and is susceptible to interruption by Met deprivation-induced SPD deficiency. Then, we explored the clinical relevance associated with this mechanism. The

clinical significance associated with GSDME-NT is difficult to explore directly for technical reasons, but we detect a negative correlation of tumor SPD level and expression of its metabolism-associated gene set (MEPO signature) with prognosis. Therapeutically, MRT effectively alters the TME to augment T cell-mediated anti-tumor immunity, an effect that is synergistically amplified when combined with cetuximab, yielding a pronounced anti-tumor response. Generally, this discovery

**Fig. 7 | Met restriction therapy boosts cetuximab efficacy via enhancing anti-tumor immunity.** (A) Effects of Met deprivation on ADCC in HONE1 and HCT116. (B) Effects of Met deprivation on HMGB1 release by ELISA in HONE1 and HCT116. (C) Immunoblot of GSDME cleavage in HONE1 and HCT116 under different conditions indicated. (D) HONE1 tumor growth in BALB/c-nu/nu mice. Mice were fed with normal diet or Met-restricted diet ( $n = 6$ ). Drug regimen is described in methods. (E) HONE1 tumor growth in BALB/c-Nu/Nu mice ( $n = 6$ ). Drug regimen is described in methods. (F) CT26-hEGFR tumor growth in BALB/c mice ( $n = 6$ ). Mice were fed with normal diet or Met-restricted diet. Drug regimen is described in methods. (G) Immunofluorescence of HMGB1 in CT26-hEGFR tumors of mice receiving indicated treatments. Scale bar: 100 $\mu$ m. (H) Quantification of nuclear HMGB1-negative cells shown in (G) ( $n = 6$ ). (I) Activated DC cell infiltration in CT26-hEGFR

tumor of mice receiving indicated treatments ( $n = 5$ ). (J) CD8<sup>+</sup> T cell tumor infiltration in CT26-hEGFR tumor of mice receiving indicated treatments ( $n = 5$ ). (K and L) Percentage of IFN- $\gamma$ <sup>+</sup> (K) and TNF- $\alpha$ <sup>+</sup> (L) CD8<sup>+</sup> T cell in CT26-hEGFR tumors of mice receiving indicated treatments ( $n = 5$ ). (M) The signaling transduction pathway related to Met-mediated pyroptotic resistance, clinical relevance and potential applications are illustrated. This figure was created in BioRender. Wu, J. (2025) <https://BioRender.com/x24v758>. Data are represented as mean  $\pm$  SD. One-way ANOVA with Tukey's multiple comparisons test (A, B, D, E, F). One-way ANOVA with Bonferroni's multiple comparisons test (H–L). NS, not significant. The results are representative of three independent experiments (A–C). Source data are provided as a Source Data file.

of the GSDME-NT pore repair mechanism not only provides insight into the interplay between Met and SPD metabolism with GSDME-mediated pyroptosis but also offers a novel avenue to enhance the efficacy of existing cancer therapies.

Current research of pyroptosis is exploding, but little attention has been paid to downstream events after gasdermin cleavage, particularly pyroptotic pore repairment. Several mechanisms have been implicated in membrane repair. In the context of pyroptosis, well-documented repair mechanisms include the ESCRT-III machinery-mediated membrane shedding of pores and pore-induced alteration of membrane phosphoinositide balance leading to self-closing pore<sup>8,40</sup>. Herein, we reveal an alternative repair pattern, in which GSDME-NT undergo endocytosis into endosomes and are subsequently delivered to lysosomes for degradation. Moreover, Met and SPD metabolism, and MYO6-mediated endocytosis is involved in this pattern. Conventionally, SPD and its derivative are involved in various molecular processes, including chromatin remodeling, RNA processing and translation<sup>41–43</sup>. These actions further affect multiple biological processes, such as autophagy, OXPHOS and histone acetylation under acidosis, enabling tumor cells survive against various stresses<sup>25,42,43</sup>. Our findings broaden this understanding by demonstrating that SPD modulates endocytosis-dependent degradation of GSDME-NT via its uncanonical function. To be specific, SPD acts as a ligand for MYO6, enhancing its structural stability and binding affinity for GSDME-NT. Consequently, the formation of MYO6-GSDME-NT-AP2 endocytic complex is facilitated, enhancing GSDME-NT pore endocytosis to repair membrane damages. Met metabolic derivative dcSAM provide aminopropyl groups necessary for SPD synthesis. We validate that Met restriction could effectively disrupt endocytic degradation of GSDME-NT via lowering SPD level. A recent study reports that taurine, a metabolic derivative of Met, takes a protective osmotic effect to inhibit membrane rupture against pyroptosis<sup>44</sup>. However, despite the membrane remaining unruptured, cells can still lose viability and die due to the persistence of osmotic crisis induced by pores, even under the action of osmotic pressure stabilizer<sup>45</sup>. The Met-SPD axis-mediated endocytic degradation of GSDME-NT reported in our study represents a rapid response for membrane pore repairment. Thus, we consider that these two mechanisms are complementary and conducive to cell survival under pyroptotic conditions.

The elucidation of the repair mechanism for GSDME-NT pores could potentially clarify the biological impacts of SPD and MYO6 on health and disease. SPD is known to possess anti-inflammatory properties, as evidenced by the inhibited secretion of proinflammatory cytokines by high level of SPD in numerous pathophysiological settings. This effect is partially attributed to the induction of autophagy because autophagy has broad anti-inflammatory effects<sup>46</sup>. The release of inflammatory mediators constitutes one of the most distinctive biological outcomes of pyroptosis. Our data demonstrate the inhibition in GSDME-NT-mediated pyroptosis by SPD, shedding further light on its anti-inflammatory mechanism. With regard to MYO6, mutations in this gene have been linked to human deafness. Specifically, the nonsense mutation (R1166X) results in a loss of cargo binding due to

the deletion of the C-terminal 120 amino acids within the CBD region of MYO6<sup>47</sup>. Concurrently, GSDME was initially discovered as a deafness gene, with mutations implicated in cell death as a disease mechanism<sup>48,49</sup>. Mutated GSDME exhibits a shortened C-terminal domain, which affects the normal shielding of its activation region by the folding back of the C-terminal domain, thereby inducing an inappropriate initiation of cell death<sup>48,49</sup>. Our results display an interaction between CBD region of MYO6 and GSDME-NT, suggesting the possibility of MYO6 dysfunction promoting GSDME-NT-mediated pyroptosis to induce deafness.

MRT represents a dynamic research frontier in oncology. The therapeutic rationale is rooted in the heightened dependency of various tumor cell lines on exogenous Met, a phenomenon often referred to as 'Met addiction'<sup>46</sup>. By constraining Met availability, tumor cells are deprived of a critical nutrient essential for their proliferation and survival. In contrast, normal cells, with their comparatively lower Met demands, can leverage alternative metabolic pathways<sup>48,50</sup>. Thus, MRT can be selectively lethal to tumors, thereby minimizing collateral damage to normal tissues. As Met is an essential amino acid necessitating dietary supplementation, dietary Met restriction represents a primary means of MRT implementation. However, patient compliance issues may present challenges to practicality of this regimen. Our study identifies SLC7A5 as a crucial Met transporter. JPH203, a compound designed based on the structure-activity relationship of SLC7A5 ligand, exhibits a safety profile comparable to that of placebo in a phase II clinical trial<sup>51,52</sup>. Our in-vivo assays reveal that inhibition of SLC7A5 function with JPH203 mirrors the anti-tumor effect of dietary Met restriction, proposing a more clinically feasible approach to MRT implementation.

Our study demonstrates an extended application of MRT, in which its combination with EGFR mAb Cmax triggers a potent tumor clearance. EGFR mAb is a widely used treatment for tumors exhibiting high level of EGFR expression, such as NPC and CRC. The primary mechanism of action lies in the inhibition of EGFR-ligand interaction, thereby impeding the activation of the RAS-ERK signaling pathway and consequently, tumor proliferation<sup>53</sup>. Nevertheless, emerging data suggest an additional role for EGFR mAbs in orchestrating immune responses via NK cell-mediated ADCC, a facet that significantly contributes to their anti-neoplastic activity<sup>54</sup>. Intriguingly, we find that it is via augmenting ADCC response that MRT enhances Cmax efficacy. Additionally, Met deficiency further promotes ADCC-induced pyroptosis, leading to DC activation and enhancing infiltration and functionality of CD8<sup>+</sup> T cells. This combined therapeutic approach holds potential in mitigating the intrinsic tumor resistance to Cetuximab, such as KRAS mutations. In summary, MRT plus cetuximab can amplify both innate and adaptive anti-tumor immunity, thus representing a promising cancer treatment strategy.

## Methods

### Study approval

Our study garnered approval from the institutional ethics review boards of Sun Yat-sen University Cancer Center (20221123180 3000502607), and all patients provided written informed consent to



participate in the study. The animal experiments conducted were approved by the experimental animal ethics committee of Sun Yat-sen University (SYSU-IACUC-2022-000189).

### Clinical specimens

A total of 220 paraffin-embedded NPC samples were collected for the purpose of conducting a survival analysis. These samples were obtained from the Sun Yat-sen University Cancer Center (Guangzhou, China), spanning the period from 2005 to 2022. None of the patients included in this study had received any form of anti-tumor therapy prior to the collection of the samples. Additionally, the tumor-node-metastasis (TNM) stages were reclassified based on the 8th edition of the American Joint Committee on Cancer (AJCC) Cancer Staging Manual. Patients' clinical characteristics were showed in the Supplementary Table 4. Sex was not considered as a biological variable. Our human included both sexes. The Institutional Ethical Review Boards of Sun Yat-sen University Cancer Center approved this study (202211231803000502607).

### Animal experiments

Female BALB/c-nu/nu and BALB/c mice, aged between 4 to 6 weeks, were procured from the Guangdong Medical Laboratory Animal Center (Foshan, China). These mice were subsequently housed in specific pathogen-free conditions at the Animal Experiment Center of Sun Yat-Sen University. All animal experiments conducted as part of this study received approval from the Animal Care and Use Committee of Sun Yat-Sen University. Mice were housed in temperature-controlled pathogen-free conditions (around 20 °C, 40% humidity) under a 12-h light/dark cycle. The maximum diameter of tumor mass allowed by ethics committee was 2\*2 cm and was not exceeded in our experiments. After a period of 5 days following the inoculation of HONE1, GSDME-NT-sh<sup>Tet-On</sup> HONE1 or CT26-hEGFR cells (at a density of 1×10<sup>6</sup> cells per mouse), the mice were randomly assigned to treatment with control treatment (normal saline), cisplatin (5 mg/kg, i.p, twice a week), MRD (0.12% Met), Dox (0.05% in the drinking water renewed every 2-3 days), JPH203 (50 mg/kg, i.p, 5 days a week), cetuximab (1 mg/mouse, i.p, twice a week), Cetuximab F(ab')<sub>2</sub> (1 mg/mouse, i.p, twice a week), DFMO (0.5% in the drinking water renewed every 2-3 days). For MRD arrangement, customized feed was purchased from Dyets Biotechnology (Wu Xi, China) and used to feed BALB/c-nu/nu and BALB/c mice on day 5 after inoculation,

### Cell lines

The human NPC cell lines HONE1 and HK1, human CRC cell line HCT116 and mouse colon cancer cell CT26 were provided by Professor Mu-Sheng Zeng and Professor Wuguo Deng at Sun Yat-sen University Cancer Center (Guangzhou). HEK293T cells were obtained from the American Type Culture Collection (ATCC). All cell lines were cultured in RPMI-1640 medium or DMEM (Corning or Boster) supplemented with 15% foetal bovine serum (FBS; ExCell Bio) and 100 U/ml penicillin-streptomycin. For starving tumor cells of individual amino acid, them were culture in customized 1640 medium (Boster).

**Lentivirus-mediated gene transfer.** HEK-293T cells were co-transfected with pSPAX2, pMD2G, Psin-e2f vector coding EGFR, MYO6 and its truncated mutant, plenti-teton-hGC vector coding GFP-GSDME-NT, GFP-GSDME and mCherry-GSDME-NT. Eight hours after transfection, the culture medium was changed to Lonza Ultra-culture medium. 48 h later, the cell virus supernatant was harvested, tittered, and used to infect indicated cells overnight. In order to screen for successful infection, puromycin (1 µg/ml) or blasticidin (5 µg/ml) were employed.

**Short interfering RNAs transfer.** The short interfering RNA were designed (Supplementary Table 5) and synthesized by GenePharma

(Shanghai, China). RNAiMAX (Invitrogen) was used to its transfection according to the manufacturer's instructions.

### Microscopy

To examine the morphology of pyroptotic cells, cells were seeded in the 12-well plate and subjected to indicated treatments. Static bright field cell images were captured using the Olympus BX53 microscope.

### Flow cytometry analysis

For determination of pore formation, cells were stained with PI in PBS for 5 min. For detection of human EGFR expression in cell surface, cells were stained with anti-EGFR antibody in PBS for 15 min. For detection of CD8 + T cell and activated DC cell infiltration in tumors of animal, upon preparation of Single-cell suspension from tumors, all samples were stained with Live/Dead dye (Biolegend, Zombie Aqua Fixable Viability Kit, 100×) for 15 min at room temperature before they were stained with different antibodies. Antibody against CD45, CD8, MHC-II, CD11c were diluted with fluorescence-activated cell sorting buffer, and stained cells. For intracellular cytokine staining, cells were stimulated with cell stimulation cocktail (Thermo Fisher) for 4 h at 37 °C. Then, these cells were fixed, permeabilized by using an intracellular staining kit (Invitrogen) and stained with anti-IFN-γ or anti-TNF antibody. All analyses were conducted by cytoFLEX LX. The antibodies used are listed in Supplementary Table 6.

**LDH and HMGB1 release detection.** HONE1 and HCT116 cells were cultured under indicated conditions. The supernatant was harvested for subsequent determination of LDH and HMGB1 release via [CytoTox 96® ndNon-Radioactive Cytotoxicity Assay](#) kit (Promega) and HMGB1 detection kit (Chondrex) respectively. All experiments were performed according to the manufacturer's instructions.

### Immunoblot and immunoprecipitation

For immunoprecipitation, whole-cell extracts were acquired after transfection or stimulation with appropriate ligands, followed by incubation with anti-myc beads or the appropriate antibodies plus Protein A/G (Pierce). Beads were then washed five times with low-salt lysis buffer, and immunoprecipitates were eluted with 2× SDS Loading Buffer (Cell Signaling Technology) and resolved by SDS-polyacrylamide gels, and then transferred to NC membranes. According to the manufacturer's recommended dilution, primary antibodies were used. Peroxidase conjugated secondary antibody (CST) was used, and the antigen-antibody reaction was visualized by enhanced chemiluminescence assay (ECL, Thermo). The antibodies used are listed in Supplementary Table 6. The unprocessed scans of the Immunoblot are provided in the Source data.

### RNA extraction, RT-qPCR

RNA extraction was conducted with the AllPrep RNA/DNA Mini Kit (Qiagen). Complimentary DNA was produced using random primers and M-MLV reverse transcriptase (Promega). The qRT-PCR assay was conducted on the Bio-Rad SPX (96 or 384) system with a 2X SYBR Green mix (Vazyme). The data were normalized to the expression of GAPDH. The sequences of the primers are synthesized by Tsingke (Beijing, China) and listed in Supplementary Table 5.

### Metabolite determination

For xenograft mouse tumors, they were pulverized in liquid nitrogen and weighed out for metabolite extraction using ice cold extraction solvent (80% methanol/water, 1 ml). Tissue was then homogenized with a homogenizer to an even suspension, and incubated on ice for an additional 10 min. The extract was centrifuged at 20,000 g for 10 min at 4 °C. For mouse serum, 50 µl of sample was mixed with 450 µl methanol containing internal standard 1 (ISI; Human Metabolome Technologies (HMT), Tsuruoka, Japan; used to standardize the



metabolite intensity) in an Eppendorf tube on ice. Subsequently, 500  $\mu\text{L}$  of chloroform was added to the above mixture and vortexed for 30 seconds, 200  $\mu\text{L}$  of ultrapure water was added and vortexed for 20 seconds, and then the mixture was centrifuged at 13000 g and 4 °C for 15 min. For cells cultured in plates, cells were placed on top of dry ice right after medium removal. 1 ml ice-cold extraction solvent (80% methanol/water) was added to each well and the extraction plate was quenched at -80 °C for 10 min. Cells were then scraped off the plate into a tube. Samples were vortexed and centrifuged as described early. All kinds of supernatant were transferred to a new tube, dried in vacuum concentrator and redissolved for HPLC-MS analysis. HPLC/MS analysis was conducted with Agilent 6495 A Triple Quadrupole LC/MS System. The temperature in the column was held constant at 35 °C. The mobile phase A and B were aqueous solution (containing 10 mM ammonium acetate, 0.1% ammonia water) and acetonitrile (containing 10 mM ammonium acetate, 0.1% ammonia water) respectively. The linear gradient was as follows: 0 min, 85% B; 1.5 min, 85% B; 5.5 min, 30% B; 8 min, 30% B; 10 min, 85% B and 12 min, 85% B. The flow rate was 0.3 ml/min. Sample volumes of 1  $\mu\text{L}$  were injected for HPLC-MS analysis. Data were processed with Agilent MassHunter Quantitative Analysis to quantify metabolites. Retention times and mass fragmentation signatures of all metabolites were validated using pure standards.

### Cellular component fractionation

Treated Cells were scraped off the plate in to tube and then washed with PBS. Plasma membrane, endosome, cytoplasmic and nuclear fraction were conducted with plasma membrane protein isolation kit (Invent Biotechnologies), endosome isolation and cell fractionation kit (Invent Biotechnologies) and NE-PER nuclear cytoplasmic extraction reagent kit (Pierce) respectively according to manufacturer's instructions.

### Immunofluorescence

For HMGB1 in-vivo determination, paraffin-embedded xenograft mouse tumors were sectioned at 3  $\mu\text{m}$  thickness. A pressure cooker performed antigen retrieval for 15-20 min in 0.01 M citrate buffer (pH 6.0). Then, sections were blocked in PBS containing 10% donkey serum or 2% bovine serum albumin for 1 hr at room temperature. Then, by using a PANO 7-plex kit (PANOVUE) according to the manufacturer's instructions, samples were incubated with dilutional primary antibodies against HMGB1. DAPI was then used to counter the nuclei. For localization of GFP-GSDME-NT WT or mutant, or GFP-GSDME-FL, cells were seeded into confocal dish, and then treated with or without Dox for indicated time. 10-min PI staining was conducted and then washed before observation. For EEA1 and Rab5 staining, cells were fixed with 4% paraformaldehyde for 15 min at room temperature, washed with PBS, and permeabilized with 0.1% Triton X-100 in PBS for 15 min. After that, cells were blocked in PBS with 2% BSA for 1 hour at room temperature and then incubated with primary anti-EEA1 and anti-Rab5 overnight at 4 °C. After washing with PBST, the cells were incubated with the corresponding secondary antibody for 45 min at room temperature. The cells were then stained with DAPI for nuclear staining. For colocalization between lysosome and GSDME-NT, indicated cells were cultured in the medium with Lyso-Tracker Green (1:15000) and DAPI for 10 min at 37 °C, then washed by PBS three times to be observed directly. All images were obtained by laser scanning confocal microscopy (LSM880, Zeiss, or Vectra Polaris) and analyzed by HALO<sup>55</sup>, Image J or Imaris 9.0 Microscopy Image Analysis Software. The antibodies used are listed in Supplementary Table 6.

**Immunohistochemical staining and scoring.** According to previous protocol<sup>56</sup>, paraffin-embedded samples were sectioned at 3  $\mu\text{m}$  thickness. A pressure cooker performed antigen retrieval for 15-20 min in 0.01 M citrate buffer (pH 6.0). Specimens were incubated with dilutional primary antibodies against SPD (1:50). Overnight at 4 °C, and the

immunodetection was performed on the following day using DAB (Dako) according to the manufacturer's instructions. Images were obtained with an AxioVision Rel.4.6 computerized image analysis system (Carl Zeiss). All sections were scored by two experienced pathologists according to the immunoreactive score (IRS) system. The IRS scores were calculated as the product of the staining intensity score and the score of percentage of positive tumor cells.

### NK cell isolation and ADCC assay

NK cells were isolated from previously frozen peripheral blood mononuclear cells via NK cell isolation kit (stem cell) according to the manufacturer's instructions and cultured in RPMI 1640 media with IL-2 (10 ng/ml) and IL-15 (10 ng/ml).  $2.0 \times 10^4$  target cells cocultured with  $10 \times 10^4$  NK cells upon cetuximab (60  $\mu\text{g}/\text{ml}$ ) and/or other drug treatment. After 6-hour incubation, they were harvested and washed by PBS to stain anti-CD56 and PI for ADCC determination.

### F(ab')<sub>2</sub> fragments generation

F(ab')<sub>2</sub> fragments of cetuximab were obtained using F(ab')<sub>2</sub> preparation Kit (Thermo Scientific) according to the manufacturer's instructions. Briefly, cetuximab was incubated with immobilized pepsin for 4 h at 37 °C to produce F(ab')<sub>2</sub> fragments and numerous small peptides of the Fc portion. To separate undigested IgG from F(ab')<sub>2</sub> fragments, the crude digest was loaded into a column with protein A and then analyzed by SDS-PAGE. The concentration of F(ab')<sub>2</sub> fragments was determined with BCA (Thermo Scientific).

**Duolink in situ PLA.** Cells were treated with or without Dox for 12 h. To detect interaction between SPD and MYO6 by Duolink analysis, fixation and permeabilization were performed as described in immunofluorescent part. Cells were then subjected to mouse anti-FLAG antibody and rabbit anti-SPD antibody. Then, cell samples were incubated with PLUS and MINUS PLA probes (Sigma-Aldrich), and PLA probes were amplified with DNA polymerase. The signals were detected by Duolink in situ detection reagent green (Sigma-Aldrich). All images were obtained by laser scanning confocal microscopy (LSM880, Zeiss, or Vectra Polaris).

### Preparation of SPD FG beads and affinity purification of SPD FG beads

Immobilization of SPD on NHS FG magnetic beads (Thermo Scientific) and its affinity purification assay were carried out according to the manufacturer's instruction. After being washed with ice-cold 1 M hydrochloric acid, beads were incubated with 5 mM SPD for 2 h at room temperature. Next, beads were washed by 0.1 M glycine (pH 2.0) and then ultrapure water. 3 M ethanolamine (pH 9.0) was added to the beads for further 2-hour incubation at room temperature. Finally, undergoing washing by purified water and storage buffer (50 mM borate, pH 8.5 with 0.05% sodium azide), beads were stored with storage buffer as 4 °C until ready for use. Cell lysates were incubated with 25  $\mu\text{L}$  of beads for 1-2 hours at room temperature on a rotator. As a negative control, SPD was added to the lysate to 2 mM for 1 hour competition at 4 °C before incubation with the SPD beads. After washing by TBST and ultrapure water, elution buffers (20 mM Hepes (pH 7.9), 100 mM NaCl, 1 mM MgCl<sub>2</sub>, 0.2 mM CaCl<sub>2</sub>, 0.2 mM EDTA, 0.1 mM DTT, 0.1% NP-40, 10% (v/v) glycerol) containing 2 mM of SPD were mixed thoroughly with the bead followed by 1 hour incubation at 4 °C on a mixer for elution.

### BLI experiment

The interaction between MYO6 and SPD was scrutinized in a real-time setting at 25 °C, utilizing the ForteBio Octet-Red96 system according to manufacturer's instructions. Briefly, biotinylated-MYO6 was loaded onto streptavidin biosensors (ForteBio). To determine binding kinetics, four SPD concentrations prepared in PBS were pipetted into a 96-

well microplate, with the remaining wells filled with PBS to serve as a negative control. Each well contained a total volume of 200  $\mu$ L. The experimental protocol included a 180 s baseline stabilization in PBS, followed by a 300 s association phase with the SPD solution, and concluding with a 180 s dissociation segment in PBS. This cycle was conducted for each SPD concentration using both an RBD-loaded sensor and a blank control sensor. Data was aligned using baseline signal and curves in FortéBio's data analysis software.

**CETSA.** The CETSA was performed essentially following the published protocol<sup>57</sup>. Briefly, cells were washed with PBS three times and collected. Samples were frozen in liquid nitrogen, and subjected to two freeze-thaw cycles to lyse the cells. The soluble portion (lysate) is separated from the cell fragments by centrifugation at 20000  $\times$  g at 4 °C for 20 minutes. Dilute the cell lysate with an appropriate buffer and divide it into two parts, one treated with 5 mM SPD and the other treated with ultrapure water (control). The sample of each group (50  $\mu$ L per tube) were then heated at indicated temperatures for 3 min in a thermal cycler (Bio-Rad) and then incubated at room temperature for 3 min. The cell lysate was centrifuged at 20,000  $\times$  g at 4 °C for 20 min, and the resulting supernatant were subjected to immunoblot analysis.

### Molecular docking

The three-dimensional structures of full length MYO6 (Uniprotkb: Q9UM54) and N terminal GSDME (Uniprotkb: O60443) are predicted by AlphaFold2. The structure of complex MYO6 and GSDME is predicted on HDock server, which automatically predicts their interaction through a hybrid algorithm of template-based and template-free docking. During the protein-protein docking process, MYO6 is set as receptor while GSDME as ligand. The top 1 predicted complex structure of MYO6 and GSDME is used for further simulation. AutoDock for GPUs version of AutoDock4.2.6 was used for molecular docking of SPD with MYO6 to obtain possible conformations and orientations of ligand at binding sites. The predicted complex structure of MYO6-GSDME is used as receptor. AutoDock4.2 used the Lamarckian Genetic Algorithm and empirical free energy scoring function and typically provided reproducible docking results for ligands. The grid parameter file of the binding pocket was created with the grid center -4.5, -1.0, -21.75 (x, y, z in Å) and dimensions 20 $\times$ 20 $\times$ 20 Å. The conformation search algorithm was carried out to explore the conformational states of a flexible ligand, using the grid maps to evaluate the ligand-protein interaction at each point in the docking simulation. The conformation with the best docking score is finally identified as the best probable conformation of MYO6-GSDME-SPD.

### Molecular dynamics simulation

MD simulations were performed with GROMACS (version 2020.6) for the complexes of MYO6-GSDME and MYO6-GSDME-SPD. AMBER Force Field parameters were used during all the simulations. The complex was neutralized by adding sodium counter ions and solvated in a box with SPC water molecules. The solvent layers between the box edges and solute surface were set to 1.2 nm. The particle mesh Ewald (PME) method was employed to treat the long-range electrostatic interactions and the calculated radius of van der Waals interaction was 1.2 nm. Before the production run, the systems were relaxed by 1000 steps using the steepest descent algorithm followed by other 1000 steps using the conjugate gradient method. For the equilibration phase, the temperature and the pressure were controlled by using the Berendsen coupling algorithm with a time constant of 0.1 and 1.0 ps, respectively. The proteins were constrained for the sake of the relaxation of water molecules in 100 ps. For the production run, an integration time step of 2 fs was employed to integrate the equations of motion. The Parrinello-Rahman coupling algorithm was used to keep the pressure constant. The simulated temperature and simulated time were set to 298.15 K and 200 ns to performed molecular dynamics

simulation of NPT ensemble in 101 kPa pressure. The binding free energy of MYO6 with GSDME was calculated with gmx\_MMPBSA (version 1.4.3) based on MMPBSA.py from AmberTools20 suit. The molecular visualizations of the 3D interaction diagrams were carried out using PyMOL software.

### Analyses based on public datasets

TCGA datasets obtained from UCSC Xena (<https://xena.ucsc.edu/>). HNSC, LUAD and ESCA cohort were used to evaluate the correlation of MEPO signature (AMD1, SRM, SMS, MTAP, ENOPH1, APIP, AGMAT, ODC1, ARG2, SMOX) to overall survival, activated DC signature<sup>58</sup> and Teff signature<sup>59</sup>.

### Quantification and Statistical Analysis

Data are presented as the mean  $\pm$  SEM or mean  $\pm$  SD of at least three independent experiments. Two-tailed Student's *t* test, one-way ANOVA with Tukey's multiple comparisons test, One-way ANOVA with Bonferroni's multiple comparisons test and two-way ANOVA with Bonferroni's multiple comparisons test were used to calculate *P* values. Survival curves were constructed using the Kaplan–Meier method, and the differences among groups were compared by the log-rank test. The two-tailed Pearson's chi-square test or Pearson's correlation analysis was used to compare clinical characteristics. The *p* value < 0.05 was considered statistically significant. All statistical analyses were performed using the SPSS version 22.0 statistical software and Graph-Pad Prism version 9.0 software.

### Reporting summary

Further information on research design is available in the Nature Portfolio Reporting Summary linked to this article.

### Data availability

All data generated and analyzed in this study are included in the article and its Supplementary Information files. TCGA datasets for HNSC, LUAD and ESCA are obtained from UCSC Xena (<https://xena.ucsc.edu/>). The mass spectrometry proteomics data have been deposited to the iProX partner repository with the dataset identifier PXD059954 and PXD060003. The other key raw data have been deposited to Research Data Deposit public platform (<https://www.researchdata.org.cn/>) with an approval number of RDDB2025874382. Source data are provided with this paper.

### References

- Kovacs, S. B. & Miao, E. A. Gasdermins: Effectors of Pyroptosis. *Trends Cell Biol.* **27**, 673–684 (2017).
- Yu, P. et al. Pyroptosis: mechanisms and diseases. *Signal Transduct. Target Ther.* **6**, 128 (2021).
- Wang, Y. et al. Chemotherapy drugs induce pyroptosis through caspase-3 cleavage of a gasdermin. *Nature* **547**, 99–103 (2017).
- Ibrahim, J., De Schutter, E. & Op de Beeck, K. GSDME: A Potential Ally in Cancer Detection and Treatment. *Trends Cancer* **7**, 392–394 (2021).
- Erkes, D. A. et al. Mutant BRAF and MEK Inhibitors Regulate the Tumor Immune Microenvironment via Pyroptosis. *Cancer Discov.* **10**, 254–269 (2020).
- Zhang, Z. et al. Gasdermin E suppresses tumour growth by activating anti-tumour immunity. *Nature* **579**, 415–420 (2020).
- Andrews, N. W. & Corrotte, M. Plasma membrane repair. *Curr. Biol.* **28**, R392–r397 (2018).
- Rühl, S. et al. ESCRT-dependent membrane repair negatively regulates pyroptosis downstream of GSDMD activation. *Science* **362**, 956–960 (2018).
- Broz, P., Pelegrín, P. & Shao, F. The gasdermins, a protein family executing cell death and inflammation. *Nat. Rev. Immunol.* **20**, 143–157 (2020).

10. Du, T. et al. Pyroptosis, metabolism, and tumor immune micro-environment. *Clin. Transl. Med.* **11**, e492 (2021).
11. Zhang, J. Y. et al. The metabolite  $\alpha$ -KG induces GSDMC-dependent pyroptosis through death receptor 6-activated caspase-8. *Cell Res.* **31**, 980–997 (2021).
12. Humphries, F. et al. Succination inactivates gasdermin D and blocks pyroptosis. *Science* **369**, 1633–1637 (2020).
13. Koppula, P., Zhuang, L. & Gan, B. Cystine transporter SLC7A11/xCT in cancer: ferroptosis, nutrient dependency, and cancer therapy. *Protein Cell* **12**, 599–620 (2021).
14. Ma, Z. et al. AhR diminishes the efficacy of chemotherapy via suppressing STING dependent type-I interferon in bladder cancer. *Nat. Commun.* **14**, 5415 (2023).
15. Li, Z. & Zhang, H. Reprogramming of glucose, fatty acid and amino acid metabolism for cancer progression. *Cell Mol. Life Sci.* **73**, 377–392 (2016).
16. Gao, X. et al. Dietary methionine influences therapy in mouse cancer models and alters human metabolism. *Nature* **572**, 397–401 (2019).
17. Kaiser, P. Methionine Dependence of Cancer. *Biomolecules* **10**, 568 (2020).
18. Sanderson, S. M. et al. Methionine metabolism in health and cancer: a nexus of diet and precision medicine. *Nat. Rev. Cancer* **19**, 625–637 (2019).
19. Mentch, S. J. et al. Histone Methylation Dynamics and Gene Regulation Occur through the Sensing of One-Carbon Metabolism. *Cell Metab.* **22**, 861–873 (2015).
20. Shilatifard, A. Chromatin modifications by methylation and ubiquitination: implications in the regulation of gene expression. *Annu. Rev. Biochem.* **75**, 243–269 (2006).
21. Rogers, C. et al. Cleavage of DFNA5 by caspase-3 during apoptosis mediates progression to secondary necrotic/pyroptotic cell death. *Nat. Commun.* **8**, 14128 (2017).
22. Rogers, C. et al. Gasdermin pores permeabilize mitochondria to augment caspase-3 activation during apoptosis and inflammasome activation. *Nat. Commun.* **10**, 1689 (2019).
23. Cullen, P. J. & Steinberg, F. To degrade or not to degrade: mechanisms and significance of endocytic recycling. *Nat. Rev. Mol. Cell Biol.* **19**, 679–696 (2018).
24. Corrotte, M. et al. Toxin pores endocytosed during plasma membrane repair traffic into the lumen of MVBs for degradation. *Traffic* **13**, 483–494 (2012).
25. Gutierrez, E. et al. eIF5A promotes translation of polyproline motifs. *Mol. Cell* **51**, 35–45 (2013).
26. Pelechano, V. & Alepuz, P. eIF5A facilitates translation termination globally and promotes the elongation of many non polyproline-specific tripeptide sequences. *Nucleic Acids Res.* **45**, 7326–7338 (2017).
27. Al-Habsi, M. et al. Spermidine activates mitochondrial trifunctional protein and improves antitumor immunity in mice. *Science* **378**, eabj3510 (2022).
28. de Jonge, J. J. et al. The MYO6 interactome: selective motor-cargo complexes for diverse cellular processes. *FEBS Lett.* **593**, 1494–1507 (2019).
29. Kruppa, A. J. et al. Myosin VI-Dependent Actin Cages Encapsulate Parkin-Positive Damaged Mitochondria. *Dev. Cell* **44**, 484–499.e6 (2018).
30. Kaksonen, M. & Roux, A. Mechanisms of clathrin-mediated endocytosis. *Nat. Rev. Mol. Cell Biol.* **19**, 313–326 (2018).
31. Kandasamy, P. et al. Amino acid transporters revisited: New views in health and disease. *Trends Biochem. Sci.* **43**, 752–789 (2018).
32. Wang, W. & Zou, W. Amino Acids and Their Transporters in T Cell Immunity and Cancer Therapy. *Mol. Cell* **80**, 384–395 (2020).
33. Bian, Y. et al. Cancer SLC43A2 alters T cell methionine metabolism and histone methylation. *Nature* **585**, 277–282 (2020).
34. Urushihara, Y. et al. AMPK/FOXO3a Pathway Increases Activity and/or Expression of ATM, DNA-PKcs, Src, EGFR, PDK1, and SOD2 and Induces Radioresistance under Nutrient Starvation. *Int. J. Mol. Sci.* **24**, (2023).
35. Seo, Y. et al. Cetuximab-mediated ADCC activity is correlated with the cell surface expression level of EGFR but not with the KRAS/BRAF mutational status in colorectal cancer. *Oncol. Rep.* **31**, 2115–2122 (2014).
36. Chew, H. Y. et al. Endocytosis Inhibition in Humans to Improve Responses to ADCC-Mediating Antibodies. *Cell* **180**, 895–914.e27 (2020).
37. Gao, W. et al. Autophagy, ferroptosis, pyroptosis, and necroptosis in tumor immunotherapy. *Signal Transduct. Target Ther.* **7**, 196 (2022).
38. Butler, M., van der Meer, L. T. & van Leeuwen, F. N. Amino Acid Depletion Therapies: Starving Cancer Cells to Death. *Trends Endocrinol. Metab.* **32**, 367–381 (2021).
39. Wang, Z. et al. Methionine is a metabolic dependency of tumor-initiating cells. *Nat. Med.* **25**, 825–837 (2019).
40. Santa Cruz Garcia, A. B. et al. Gasdermin D pores are dynamically regulated by local phosphoinositide circuitry. *Nat. Commun.* **13**, 52 (2022).
41. Lee, M. S. et al. Ornithine aminotransferase supports polyamine synthesis in pancreatic cancer. *Nature* **616**, 339–347 (2023).
42. Murthy, D. et al. Cancer-associated fibroblast-derived acetate promotes pancreatic cancer development by altering polyamine metabolism via the ACSS2-SP1-SAT1 axis. *Nat. Cell Biol.* **26**, 613–627 (2024).
43. Murthy, D. et al. The MUC1-HIF-1 $\alpha$  signaling axis regulates pancreatic cancer pathogenesis through polyamine metabolism remodeling. *Proc. Natl. Acad. Sci. USA* **121**, e2315509121 (2024).
44. El-Kenawi, A. et al. Elevated Methionine Flux Drives Pyroptosis Evasion in Persister Cancer Cells. *Cancer Res.* **83**, 720–734 (2023).
45. Calcinotto, A. et al. Cellular Senescence: Aging, Cancer, and Injury. *Physiol. Rev.* **99**, 1047–1078 (2019).
46. Madeo, F. et al. Spermidine in health and disease. *Science* **359**, eaan2788 (2018).
47. Arden, S. D. et al. Loss of cargo binding in the human myosin VI deafness mutant (R1166X) leads to increased actin filament binding. *Biochem. J.* **473**, 3307–3319 (2016).
48. de Beeck, K. O., Van Laer, L. & Van Camp, G. DFNA5, a gene involved in hearing loss and cancer: a review. *Ann. Otol. Rhinol. Laryngol.* **121**, 197–207 (2012).
49. Op de Beeck, K., Schacht, J. & Van Camp, G. Apoptosis in acquired and genetic hearing impairment: the programmed death of the hair cell. *Hear. Res.* **281**, 18–27 (2011).
50. Wanders, D., Hobson, K. & Ji, X. Methionine Restriction and Cancer Biology. *Nutrients* **12**, 684 (2020).
51. Kanai, Y. Amino acid transporter LAT1 (SLC7A5) as a molecular target for cancer diagnosis and therapeutics. *Pharm. Ther.* **230**, 107964 (2022).
52. Nishikubo, K. et al. Combination effects of amino acid transporter LAT1 inhibitor nanvuranlat and cytotoxic anticancer drug gemcitabine on pancreatic and biliary tract cancer cells. *Cancer Cell Int.* **23**, 116 (2023).
53. Ciardiello, F. & Tortora, G. EGFR antagonists in cancer treatment. *N. Engl. J. Med.* **358**, 1160–1174 (2008).
54. Wang, W. et al. NK Cell-Mediated Antibody-Dependent Cellular Cytotoxicity in Cancer Immunotherapy. *Front Immunol.* **6**, 368 (2015).
55. Chen, E. et al. FLI1 promotes IFN- $\gamma$ -induced kynurenine production to impair anti-tumor immunity. *Nat. Commun.* **15**, 4590 (2024).
56. Zhang, C. et al. HO-1 impairs the efficacy of radiotherapy by redistributing cGAS and STING in tumors. *J. Clin. Invest.* **134**, e181044 (2024).

57. Li, Z. et al. Tumor-repopulating cells evade ferroptosis via PCK2-dependent phospholipid remodeling. *Nat. Chem. Biol.* **20**, 1341–1352 (2024).
58. Yuan, X. et al. Vitamin E Enhances Cancer Immunotherapy by Reinvigorating Dendritic Cells via Targeting Checkpoint SHP1. *Cancer Discov.* **12**, 1742–1759 (2022).
59. Zheng, Y. et al. Immune suppressive landscape in the human esophageal squamous cell carcinoma microenvironment. *Nat. Commun.* **11**, 6268 (2020).

## Acknowledgements

This study was supported by grants from the National Natural Science Foundation of China (81930072 and 82172870 to JM; 82103449 to XYL; U24A20725 to LLT), Overseas Expertise Introduction Project for Discipline Innovation (111 Project, B14035 to JM).

## Author contributions

J.M., X.Y.L., L.L.T. and J.W.W. conceived the project. J.W.W., C.D., C.Q.Z., Z.M.X., Z.J.D., L.F.L., H.M.W. and T.X.H. and performed the experiments. J.W.W., C.D., C.Q.Z. developed methodology. J.W.W., C.D., C.Q.Z. performed data analysis. J.W.W., C.D., C.Q.Z., Z.M.X. and Z.J.D. contributed to clinical sample collection and analysis. J.M. wrote the manuscript.

## Competing interests

The authors declare no competing interests.

## Additional information

**Supplementary information** The online version contains supplementary material available at <https://doi.org/10.1038/s41467-025-57511-4>.

**Correspondence** and requests for materials should be addressed to Linglong Tang, Jun Ma or Xiaoyu Liang.

**Peer review information** *Nature Communications* thanks Dhiraj Bhatia and the other, anonymous, reviewer(s) for their contribution to the peer review of this work. A peer review file is available.

**Reprints and permissions information** is available at <http://www.nature.com/reprints>

**Publisher's note** Springer Nature remains neutral with regard to jurisdictional claims in published maps and institutional affiliations.

**Open Access** This article is licensed under a Creative Commons Attribution-NonCommercial-NoDerivatives 4.0 International License, which permits any non-commercial use, sharing, distribution and reproduction in any medium or format, as long as you give appropriate credit to the original author(s) and the source, provide a link to the Creative Commons licence, and indicate if you modified the licensed material. You do not have permission under this licence to share adapted material derived from this article or parts of it. The images or other third party material in this article are included in the article's Creative Commons licence, unless indicated otherwise in a credit line to the material. If material is not included in the article's Creative Commons licence and your intended use is not permitted by statutory regulation or exceeds the permitted use, you will need to obtain permission directly from the copyright holder. To view a copy of this licence, visit <http://creativecommons.org/licenses/by-nc-nd/4.0/>.

© The Author(s) 2025